

# Impact of the Boreal Summer Intraseasonal Oscillation on the Diurnal Cycle of Precipitation near and over the Island of Luzon

KYLE CHUDLER

*Department of Atmospheric Sciences, Colorado State University, Fort Collins, Colorado*

WEIXIN XU

*School of Atmospheric Sciences, Sun Yat-sen University, Zhuhai, China*

STEVEN A. RUTLEDGE

*Department of Atmospheric Sciences, Colorado State University, Fort Collins, Colorado*

(Manuscript received 2 August 2019, in final form 18 February 2020)

## ABSTRACT

During the boreal summer, satellite-based precipitation estimates indicate a distinct maximum in rainfall off the west coast of the island of Luzon in the Philippines. Also occurring during the summer months is the boreal summer intraseasonal oscillation (BSISO), a main driver of intraseasonal variability in the region. This study investigates the diurnal variability of convective intensity, morphology, and precipitation coverage offshore and over the island of Luzon. The results are then composited by BSISO activity. Results of this study indicate that offshore precipitation is markedly increased during active BSISO phases, when strong low-level southwesterly monsoon winds bring increased moisture and enhanced convergence upwind of the island's high terrain. A key finding of this work is the existence of an afternoon maximum in convection over Luzon even during active BSISO phases, when solar heating and instability are apparently reduced due to enhanced cloud cover. This result is important, as previous studies have shown in other areas of the tropics afternoon convection over landmasses is a key component to offshore precipitation. Although offshore precipitation is maximized in the evening hours during active phases, results indicate that precipitation frequently occurs over the ocean around the clock (both as organized systems and isolated, shallow showers), possibly owing to an increase in sensible and latent heat fluxes, vertical wind shear, and convergence of the monsoon flow with land features.

## 1. Introduction

The Asian summer monsoon (ASM) is a major component of the global weather system with impacts on multiple scales. During the ASM, heavy rain falls in Southeast Asia, India, and the Maritime Continent. One striking feature of the ASM rainfall climatology are maxima in rainfall just offshore of the Western Ghats of India (Grossman and Durran 1984; Krishnamurti et al. 1983), Myanmar (Xie et al. 2006; Zuidema 2003), and the west coast of the Philippines (Ho et al. 2008). The inland locations in these three regions are marked by mountain ranges that protrude along or near the coastline (Fig. 1). An obvious hypothesis is that these rainfall maxima result from orographic lifting. The

combination of strong low-level southwesterly monsoonal winds impinging on the mountain ranges in each of these locations would certainly lead to pronounced upslope flow. However, if the rainfall was purely due to upslope flow, one would expect the precipitation to predominately fall over and near the highest terrain, rather than displaced to the west over open ocean as indicated by Fig. 1. So, while orographic lifting may play some role, it alone likely cannot explain the observed precipitation patterns.

These offshore rainfall maxima have previously been examined in modeling studies. Ogura and Yoshizaki (1988) utilized a two-dimensional cloud model to examine the Western Ghats precipitation maximum. They found that both vertical wind shear and ocean surface fluxes contributed to the offshore precipitation maximum. When either of these factors were suppressed

---

*Corresponding author:* Kyle Chudler, kyle.chudler@colostate.edu

DOI: 10.1175/MWR-D-19-0252.1

© 2020 American Meteorological Society. For information regarding reuse of this content and general copyright information, consult the [AMS Copyright Policy](https://www.ametsoc.org/PUBSReuseLicenses) ([www.ametsoc.org/PUBSReuseLicenses](https://www.ametsoc.org/PUBSReuseLicenses)).

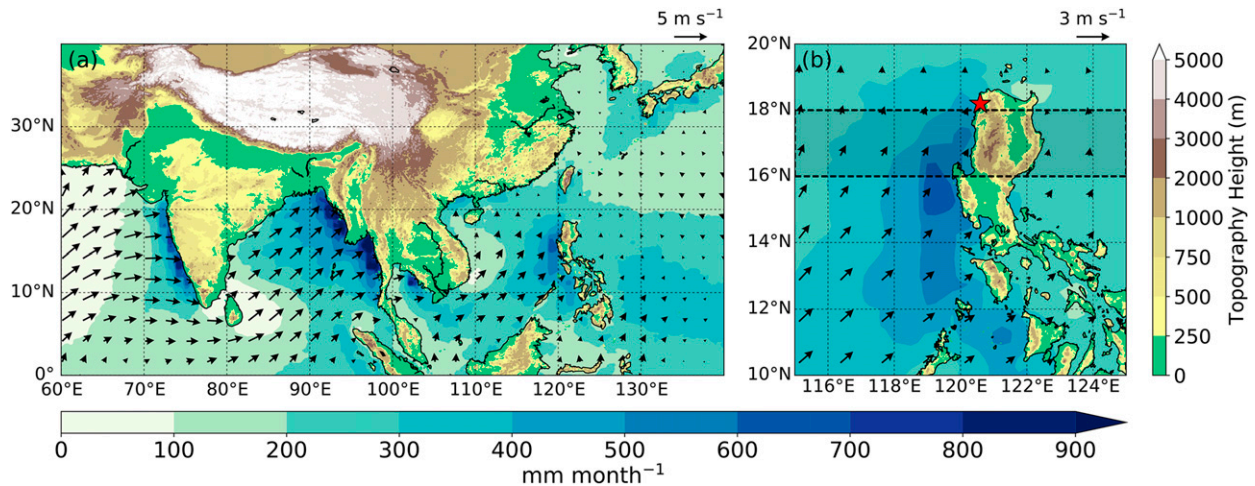


FIG. 1. Mean monthly summer precipitation (from TRMM 3B42), surface wind vectors (from CCMP), and topography elevation (from the Shuttle Radar Topography Mission) for the (a) Asian and (b) Philippines region. The longitudinal band highlighted in (b) is the area analyzed in Fig. 9. The red star in (b) is the launch location of the atmospheric soundings discussed in section 2d.

in the model simulations, the location and amount of precipitation generated by the model disagreed with observations. Only by including both a typical monsoonal wind profile (westerlies in the low levels, easterlies aloft) and ocean surface fluxes did the model simulations fall in accord with observations. In other model simulations, Xie et al. (2006) found that even the relatively small and narrow mountain ranges of Myanmar cause enough impedance of the monsoon flow to create the convergence necessary to generate convection and offshore rain.

Previous field projects have shown that the diurnal cycle is a crucial element to explaining coastal rainfall. In the Winter Monsoon Experiment (WMONEX; Houze et al. 1981), the land/sea breeze cycle was determined to be a key contribution to the offshore rain. The nighttime land breeze was shown to converge with the low-level monsoon flow to produce lift and precipitation offshore. In the Terrain-Influenced Monsoon Rainfall Experiment (TiMREX), Ruppert et al. (2013) found that katabatic drainage winds from the mountain ranges enhanced offshore flow and therefore convergence with the westerlies. And in the North American Monsoon Experiment (NAME; Lang et al. 2007; Nesbitt et al. 2008), offshore movement of land-generated convection was determined to contribute a significant fraction of the offshore precipitation. Afternoon convection formed over the Sierra Madre Occidental, and then moved westward into the Gulf of California, often in the form of mesoscale convective systems. Mapes et al. (2003) proposed a gravity wave mechanism to explain rainfall adjacent to landmasses. They argued that daytime heating over the land expands the boundary layer,

causing gravity waves to propagate away from the disturbed region. These gravity waves lead to destabilization over the adjacent waters thereby supporting convection. This was also the mechanism offered by Yokoi et al. (2017) to explain the offshore movement of convection observed near the island of Sumatra during the Years of the Maritime Continent (YMC) pilot field campaign. In this field project, a cooling (and subsequent destabilization) of potential temperature was noted in the lower free troposphere on days when offshore precipitation was greatest. This lower tropospheric cooling was attributed to anomalous upward motion caused by gravity waves, which themselves originated from earlier convection over the land. However, in the subsequent YMC field campaign in 2017, Yokoi et al. (2019) noted that although the same low-level cooling was observed in the operations area, it was not always associated with offshore convection, leading to a suggestion that gravity wave propagation may not be a sufficient condition for offshore rainfall. The authors further hypothesized that vertical wind shear was required to allow afternoon land-based convection to migrate offshore. The variety of hypotheses put forward in these studies highlights the complexity of the processes that promote offshore precipitation, and suggests that one single mechanism may not be able to explain the phenomenon in any given region (let alone across the tropics).

Closely tied to the activity of the ASM is the boreal summer intraseasonal oscillation (BSISO). A warm-season analog to the boreal winter Madden-Julian oscillation (MJO), the BSISO consists of a convective envelope propagating from the Indian Ocean to the

west Pacific (BSISO1; Lee et al. 2013; Wang and Xie 1997). Associated with this convective envelope is increased cloud cover, positive precipitation anomalies, and increased southwesterly monsoon flow. These “active” periods, as they will be referred to in this study, are punctuated by “inactive” phases, which are characterized by increased solar insolation, reduced precipitation, and reduced low-level winds. A full BSISO oscillation period is approximately 30–60 days.

Xu and Rutledge (2018) examined the variability of convection in relation to the BSISO over the South China Sea (SCS) and the Philippines. During active phases, precipitation systems were generally larger in size and contained a larger stratiform fraction, possibly due to increased vertical shear and moister midlevels. These large systems were found to be present over ocean and land, at nearly the same frequency. By contrast, inactive phases featured smaller but more intense convective systems over land. Over water, convection was less frequent compared to active phases. The contrast in the relationship of land–sea convection between active and inactive BSISO periods was explained in part by convective instability, which was found to be higher (lower) over the Philippines (SCS) during inactive periods compared to active periods.

Natoli and Maloney (2019) examined the precipitation patterns in the Philippines, and how the diurnal cycle and offshore precipitation is impacted by the BSISO. Their findings show that the amplitude of the diurnal cycle is maximized at the end of inactive periods and minimized at the end of active periods. They state that the afternoon convection over land is initiated by interactions between sea-breeze and mountain–valley circulations that are stronger during inactive periods when solar insolation is at a maximum. Furthermore, they concluded that offshore movement of afternoon convection is maximized in the transition period from inactive to active periods, and minimized during the transition from active to inactive periods. Offshore propagation of precipitating systems was attributed to gravity waves initiated by afternoon convective heating in their study.

The offshore rainfall maxima observed off the west coast of the Philippines (as well as Western Ghats and Myanmar) during the ASM are interesting features with significant impact to the coastal cities in these regions. In summary, the research objectives of this study are to 1) investigate the variability in rainfall patterns in and around the island of Luzon and how this variability is related to BSISO activity and associated atmospheric conditions and 2) based on satellite observations,

analyze the characteristics of precipitating systems in the region and evaluate how their characteristics vary throughout the day over land/sea and during inactive/active phases of the BSISO. Whereas previous studies (such as Natoli and Maloney 2019) have examined similar questions as objective 1) by looking only at surface rainfall statistics and reanalysis data, the novelty of this study is found in objective 2), where characteristics such as vertical structure, size, morphology, and intensity of precipitating features are examined. Previous studies have suggested that orographic lifting, wind-enhanced sea–air surfaces fluxes, vertical wind shear, convergence of large-scale westerlies with land breezes or convective outflows, and offshore movement of land-generated convection all play a role in producing the offshore maximum. It will be shown in this study that all of these factors are significantly influenced by BSISO activity, which in turn significantly modifies the location, frequency, and structure of precipitating systems.

#### *a. Data resources*

To study the rainfall patterns and diurnal cycle over Luzon, spaceborne radar products from the Tropical Rainfall Measuring Mission (TRMM) Precipitation Radar (PR) and Global Precipitation Measurement Ku-band Precipitation Radar (GPM KuPR) were used. One such product that is utilized is the precipitation feature (PF) database. As outlined in Liu et al. (2008), the database inputs TRMM PR data and groups together near-surface raining pixels that are contiguous in space. Once a feature is outlined, the location of the PF is determined as the centroid of an ellipse surrounding the raining pixels. In addition to the three-dimensional PR radar data, measurements from other TRMM instruments (Kummerow et al. 1998) such as the Lightning Imaging Sensor (LIS), Visible and Infrared Scanner (VIRS), and Microwave Imager (TMI) can then be collocated with the PF. Therefore, information such as area-averaged rain rate, convective area, maximum reflectivity echo heights, and total lightning count can be defined for each PF. The date and time of the PF occurrence was also recorded, which allowed for PF statistics to be composited by time of day (diurnal cycle) or date of occurrence. A similar database is also available for GPM precipitation features (although without the lightning information from LIS). Over 100 000 PFs were compiled and analyzed in the present analysis, over 90% of which were from TRMM (due to its longer data collection period).

The TRMM and GPM PF databases provides an overview of precipitation frequency, intensity, and morphology. However, although PFs can be very large and span over

both open ocean and the nearby mountainous terrain in this region, just a single value of mean rain rate, maximum echo lightning height, total flash count, etc. are given for an entire PF. Because of this, the distinction between land- and sea-based precipitation can often be blurred when looking at PF statistics. To resolve this issue, high-resolution orbital radar data ( $5\text{ km} \times 5\text{ km}$  horizontal resolution at the nadir of each scan) from the TRMM PR (2A25 version 7, [Iguchi et al. 2000](#)) and GPM KuPR (2A version 5, [Iguchi and Meneghini 2016](#)) are analyzed. The Ku-band radar on GPM is an updated version of the PR radar on TRMM, and operates at the same frequency, so measurements from the two instruments are taken to be consistent with one another. These datasets provide radar measurements with sufficient detail to accurately resolve the salient differences between land and ocean precipitation. Importantly, these products also provide vertical profiles of radar reflectivity (TRMM 250-m and GPM 125-m resolution). Previous studies in the region using only surface rainfall estimates (i.e., [Natoli and Maloney 2019](#)) cannot provide information on the vertical structure of storms, so this is a novel component of this research. While surface rainfall statistics are sufficient to determine the patterns of where and when rain occurs, the question of “how” it rains (i.e., what are the characteristics of the system that produces the rain) is equally important as it has implications on the water/energy budget in the region. Over 4500 radar overpasses (each 250 km wide) were used in total, with approximately equal sampling of inactive and active BSISO phases (defined below). For analysis, the TRMM PR and GPM KuPR rain rate data were interpolated onto a  $0.5^\circ \times 0.5^\circ$  grid by taking the mean of all rain rate measurements in a given grid box.

The TRMM dataset from the University of Washington (TRMM UW; [Houze et al. 2015](#)) was also utilized in this study. Like the TRMM PF dataset, contiguous raining pixels are grouped into precipitation features. The advantage of the TRMM UW dataset is that features are also classified into different categories based on their areal coverage and intensity. Specifically, features are identified as follows:

- Isolated shallow echo: Features whose radar echoes extend no higher than 1 km below the freezing level.
- Deep convective cores: Convective features with reflectivities greater than 30 dBZ and an echo-top height of at least 8 km. Note the 30-dBZ contour is not required to extend beyond 8 km.
- Wide convective cores: Convective features with reflectivities greater than 30 dBZ and a horizontal

area of at least  $800\text{ km}^2$ . Note the 30-dBZ contour is not required to pass the area threshold.

- Broad stratiform regions: Stratiform features with a horizontal area of at least  $40\,000\text{ km}^2$ .

In the above definitions, the convective and stratiform designations are determined by the TRMM 2A23 rain-type product. The “moderate” thresholds for categorizing features is presented above, although a “strong” threshold is also available. However, features that pass the stronger thresholds are rarely observed in the Maritime Continent ([Houze et al. 2015](#)). Thus, the moderate threshold features were used in this study. By combining this feature classification dataset with the gridded TRMM 2A25 dataset (also included in TRMM UW), the frequency of occurrence for the different feature categories were tabulated according to both space and time.

The BSISO drives changes in wind regimes between inactive and active phases around Luzon. The Cross-Calibrated Multi-Platform (CCMP; [Atlas et al. 2011](#)) wind retrieval product was used to obtain historical gridded wind data over the study region. CCMP utilizes a variational analysis method (VAM) to combine wind measurements from moored buoys and several microwave radiometers and scatterometers with reanalysis data from the European Centre for Medium-Range Weather Forecasts interim reanalysis (ERA-Interim) database. From this, global  $0.25^\circ$  gridded 6-hourly wind vector estimates are produced. By combining rainfall information from TRMM and GPM with wind estimates from CCMP, a detailed picture of variability between BSISO phases can be established.

An understanding of intraseasonal variability in atmospheric variables, which modulate convection, is also desired. The European Centre for Medium-Range Weather Forecasts interim reanalysis (ERA-Interim) dataset ([Dee et al. 2011](#)) from 1998 to 2017 was used to examine the climatological values of convective available potential energy (CAPE), vertical wind shear, sensible and latent heat fluxes, and solar radiation across different BSISO phases. Only climatological and satellite data from June to September are included in the analysis, which corresponds to periods when the monsoon and BSISO signal are typically strongest.

#### *b. BSISO phase selection*

This research intends to examine the differences in precipitation characteristics between inactive and active BSISO periods. Accordingly, the index defined by [Lee et al. \(2013, hereafter L13\)](#) was used to determine the phase and amplitude of the oscillation. Typically, historical BSISO indices are calculated by first applying a

25–90-day bandpass filter to the OLR and U850 hPa fields. One advantage of the L13 index is that real-time indices can be calculated without having to apply bandpass filtering to the real-time OLR or U850 data. It is this nonfiltered, real-time index that will be utilized for the purposes of this study. The justification for this choice lies in the ability of the real-time index to better capture the day-to-day variability in the study region. Because this study examines precipitation on a diurnal time scale, the short-term variability in atmospheric conditions captured by the real-time L13 index is more relevant than the intraseasonal variability captured by a time-filtered index. In other words, the smooth progression of single BSISO events across the entire ASM region is not particularly important here, and using the real-time index provides a way to classify individual days as inactive or active, without the influence of other days. Averages of 500-mb geopotential heights and surface precipitation composited over BSISO phases using smoother indices like the OLR MJO index (OMI; Kiladis et al. 2014) or the smoothed L13 index (not shown) do not display the same contrast between inactive and active phases as when composited using the real-time L13 index. The real-time L13 index was utilized in Xu and Rutledge (2018) and was able to adequately capture the influence of daily large-scale variability on convection.

To include only days with a strong BSISO signal, days when the L13 index amplitude was less than 1 were excluded from the analysis. Additionally, days where the BSISO phase was 4 or 8 were not included, as these represent the transition period between the inactive (phase 1–3) and active (phase 5–7) periods.

### c. Statistical significance

For this study, the statistical significance of the difference between mean reanalysis and precipitation fields during inactive and active phases was calculated using a two-tailed Student's *t* test, with the null hypothesis being that the two-sample means were drawn from the same distribution. Autocorrelation in the data was accounted for through choosing an effective sample size based on the *e*-folding time scale of the data (Leith 1973).

## 2. Results

### a. Overview

The following sections describe the characteristics and location of precipitation over Luzon and the surrounding ocean during different phases of the BSISO. First, environmental conditions associated with inactive and

active BSISO phases are examined with reanalysis data. Rainfall and TRMM UW echo feature variation between inactive and active phases of the BSISO will also be presented, along with TRMM UW echo feature statistics. Next, the diurnal cycle of rain will be discussed, both in the context of surface rainfall and characteristics of precipitation features. The vertical structure of convective systems during inactive and active phases will then be assessed using reflectivity profiles from the TRMM PR and GPM KuPR radars. Finally, several individual GPM KuPR overpasses will be highlighted to provide examples of what convection is expected to typically look like in the region.

### b. Intraseasonal variability

#### 1) REANALYSIS DATA

Figure 2 shows the June–September mean 500-hPa geopotential height and 850-hPa wind vectors during each phase of the BSISO. During inactive phases (phase 1–3), the flow was dominated by the Western Pacific subtropical high to the NE of the study region. Peaking in strength and westward extent during phase 3, this high strengthened and even acted to reverse the southwesterly monsoon flow at low levels. This high geopotential height center shifts eastward away from the Philippines in phase 4, and in phase 5, a low 500-hPa geopotential height center is situated over the SCS, accompanied by strong low-level southwesterlies. This marks the beginning of the active phases (5–7). As this zone of low geopotential height expands eastward and northward in phases 6 and 7, the monsoon flow strengthens over the region. The strongest winds ( $12\text{--}14\text{ m s}^{-1}$ ) were noted in the southern half of the region, where the pressure gradient is greatest.

Figure 3 shows the difference in several ERA-Interim reanalysis fields between inactive and active BSISO phases. Mean solar radiation was  $100\text{--}200\text{ W m}^{-2}$  higher during inactive phases across the grid, due to decreased cloud cover in comparison to active phases. Over ocean, latent and sensible heat fluxes were highest during active phases. Ogura and Yoshizaki (1988) showed that these fluxes were important for offshore precipitation. The increase in surface fluxes can be explained through the bulk equations for sensible heat ( $S_H$ ) and latent heat ( $L_H$ ) fluxes:

$$S_H = C_H U (T_s - T_a),$$

$$L_H = C_E U (q_s - q_a),$$

where  $C_H$  and  $C_E$  are transfer coefficients (which depend on physical parameters of the fluid like friction

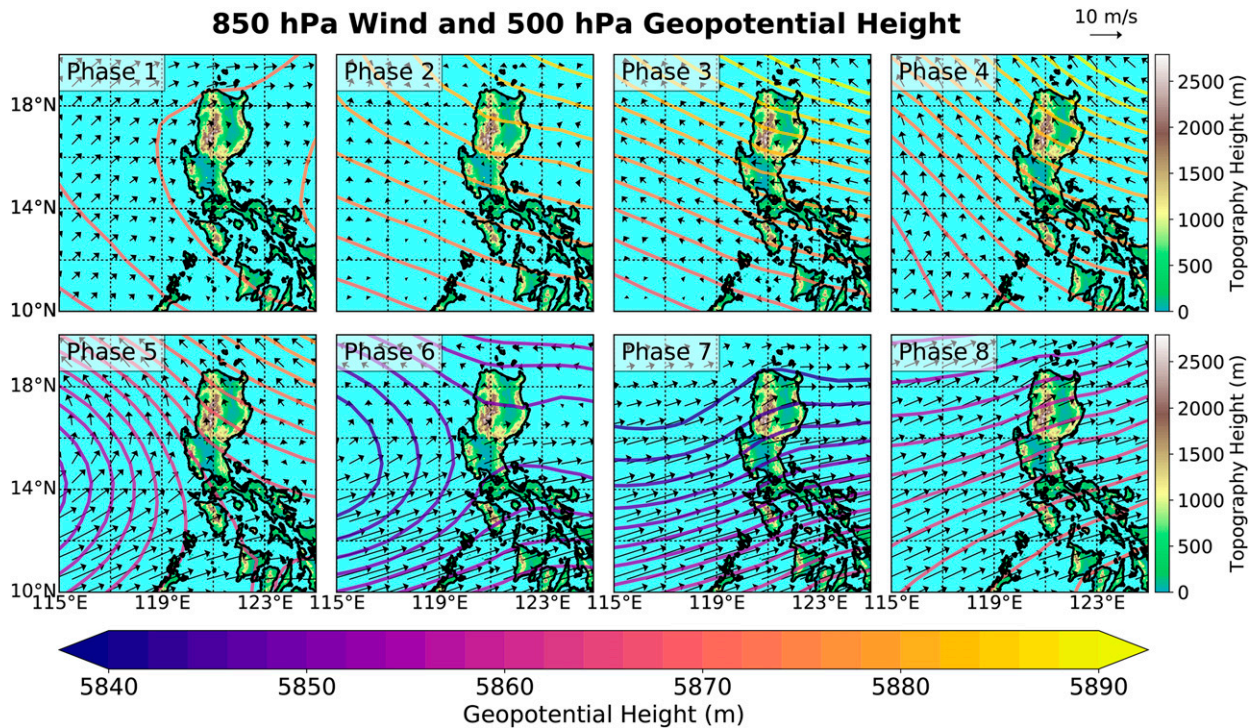


FIG. 2. Mean 850-hPa winds (vectors) and 500-hPa geopotential heights (contours) from ERA-Interim reanalysis across different BSISO phases.

velocity, roughness length, and von Kármán constants, and are treated as constants here),  $U$  is the surface wind speed,  $T$  is temperature,  $q$  is the specific humidity, and the subscripts  $s$  and  $a$  represent variables at the land/ocean surface and 10-m height, respectively (Wang et al. 1996). Because land and sea surface temperature (which also controls  $q_s$ ) only changed by a less than  $1^\circ\text{C}$  between inactive and active phase (according to ERA reanalysis, not shown), and surface wind speed more than doubles in places, the change in  $U$  dominates changes in  $S_H$  and  $L_H$ . Since low-level winds were considerably stronger during active phases [see section 2b(2)], sensible and latent heat fluxes were much greater over the ocean during active phases. Specifically, the mean sensible (latent) heat flux over water during active phases was  $4.6 \text{ W m}^{-2}$  ( $39.8 \text{ W m}^{-2}$ ) higher than during inactive phases (Fig. 3), an increase of 56% (40%). Over land, the inverse was true. Greater solar insolation during inactive phases warmed the land and generated a sharper temperature gradient, leading to larger sensible heat fluxes ( $9.6 \text{ W m}^{-2}$ , 25% increase). Furthermore, a drier boundary layer promoted greater latent heat fluxes, although to a lesser degree ( $7.5 \text{ W m}^{-2}$ , 5% increase).

Over land, CAPE was up to  $300 \text{ J kg}^{-1}$  higher during inactive phases than during active phases, consistent

with reduced cloud cover and increased solar insolation. This instability was conducive to the development of afternoon convection during inactive phases, as shown in Xu and Rutledge (2018). Over the ocean, there was an apparent increase in instability during active phases. This may be due to the increase in surface energy fluxes during active phases. An increase in sensible heat and latent heat flux from the ocean surface would act to increase low-level temperature and moisture, respectively, thereby increasing CAPE (assuming the mid- to upper troposphere was invariant). Low-level moisture convergence has previously been shown to be correlated with instability in the region (Johnson and Ciesielski 2013; Petersen et al. 1996), so the increase in 700-hPa relative humidity (also plotted in Fig. 3) is consistent with the increase in CAPE. It should be noted that instability metrics like CAPE have been shown to be only weakly correlated with oceanic convection in the tropics (Mapes and Houze 1992; Lucas and Zipser 2000; Peters et al. 2013). However, over land, the impact of CAPE is likely more pronounced. Increased CAPE was directly attributed to the increase in intense convection over Luzon in Xu and Rutledge (2018), and the modeling study of Dellaripa et al. (2020) showed a correlation between the timing of

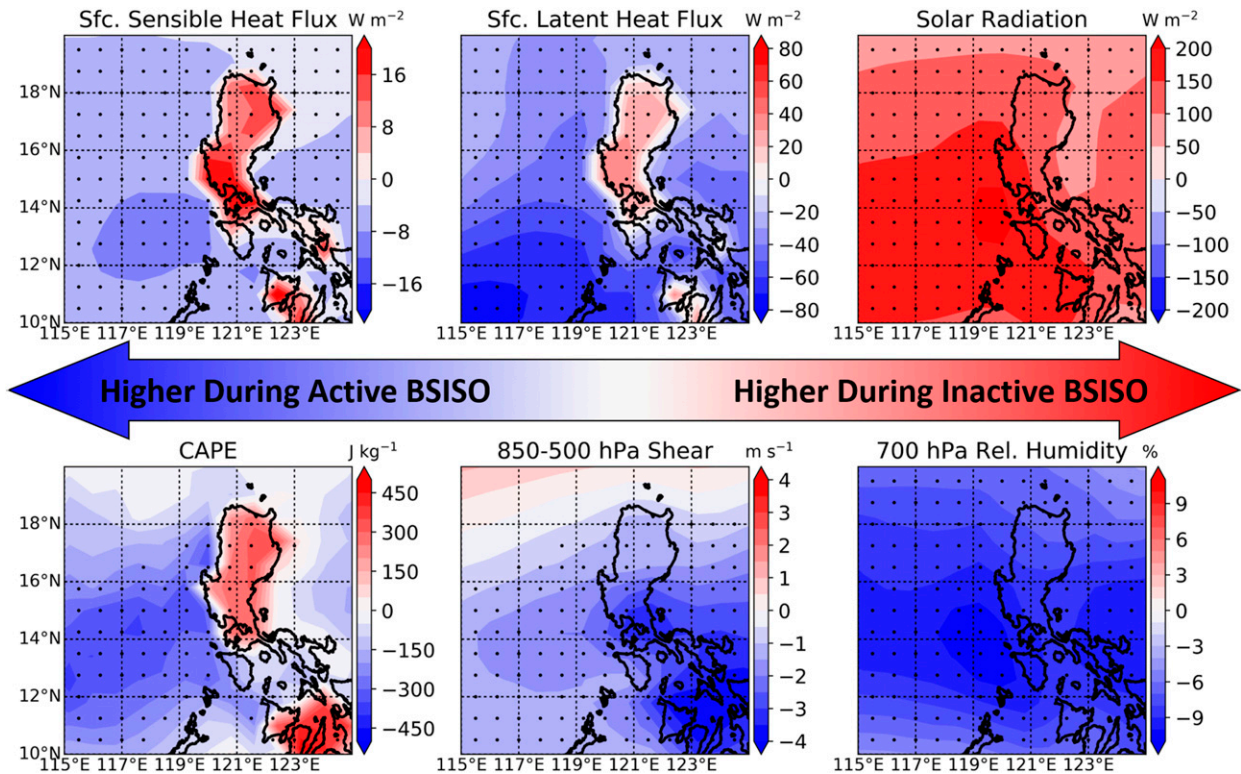


FIG. 3. Inactive-active difference in ERA-Interim reanalysis data for upward sensible heat flux, upward latent heat flux, downwelling solar radiation, CAPE, accumulated from the near-surface level (1000 hPa over the ocean, 925 hPa over land) to the level of neutral buoyancy, 800–500-hPa wind shear, and 700-hPa relative humidity. Solar radiation values at night (zeros) were ignored in calculating the mean. Stippling denotes significance at a confidence level of 95%.

instability generation and peak diurnal rainfall in Luzon. So, although CAPE may not be the most important metric for precipitation generation in this region, the diurnal variability of instability over land still has been shown to modulate the intensity and timing of afternoon convection.

Vertical wind shear across various depths was also examined with the reanalysis data. Vertical wind shear was found to be higher during active BSISO phases at midlevels (850–500 hPa), as well as in a deep layer (700–150 hPa) and at low levels (10 m–850 hPa, not shown). During active phases, strong low-level southwesterlies (monsoonal flow) are situated below enhanced upper-level easterlies, increasing the vertical wind shear. Low-, mid-, and deep-layer shear has been shown to be important to the development and maintenance of mesoscale convective systems (Alfaro and Coniglio 2018; Coniglio et al. 2006; Lang et al. 2007; Moncrieff and Liu 1999; Saxen and Rutledge 2000; Thorpe et al. 1982; Zheng et al. 2013). Thus, higher values of vertical wind shear may aid isolated terrain-based convection in growing upscale and advancing offshore. This agrees with the results of Ogura and Yoshizaki

(1988), which linked greater wind shear with increased offshore precipitation.

## 2) RAINFALL AND SURFACE WINDS

Mean surface rain rate from TRMM PR and GPM KuPR was composited into inactive and active periods (Fig. 4). Mean CCMP surface wind vectors during inactive and active phases are also plotted. Active phases featured a strong southwesterly monsoonal flow across most of the domain, especially the southern portions. In the northern part of the domain, the flow weakened and turned more northerly as it wrapped around the monsoon low in the SCS during active phases. During inactive phases, the flow was much weaker and generally southerly or nondirectional. Influence of the western Pacific subtropical high is noted to the east and northeast of Luzon, where the flow had a slight easterly component.

The domain-mean rain rate during active phases was more than double that of inactive phases (0.57 vs 0.27 mm h<sup>-1</sup>). During inactive phases, a clear precipitation maximum was apparent over the high terrain of Luzon. Precipitation was also situated over the ocean, but with reduced intensity and frequency compared to

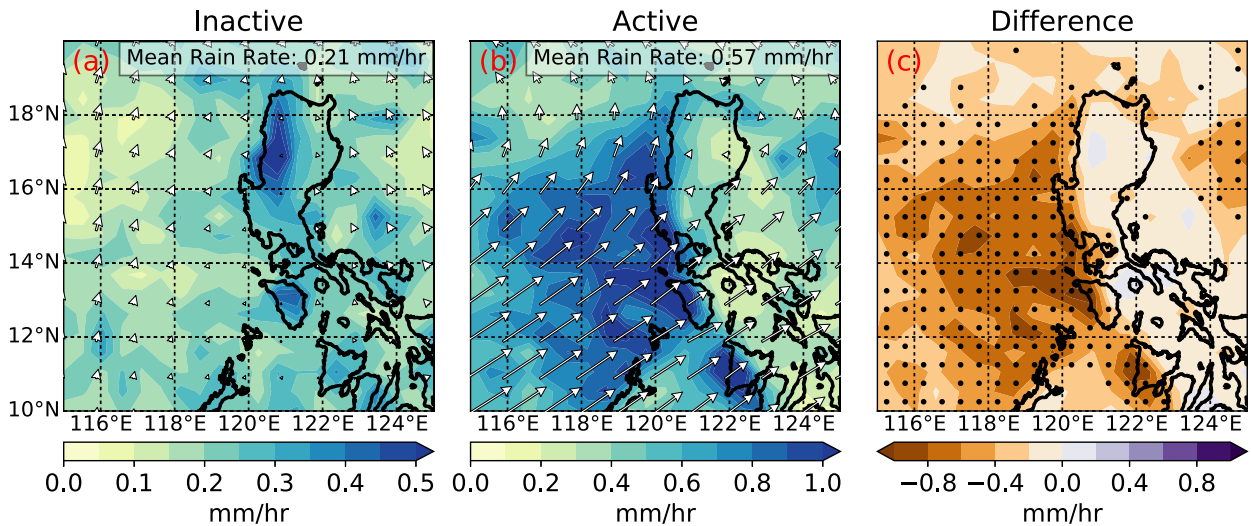


FIG. 4. Unconditional mean rain during (a) inactive and (b) active BSISO phases, and (c) the inactive–active difference. Vectors in (a) and (b) are mean surface wind vectors from CCMP. Stippling in (c) denotes significance in the precipitation difference field at confidence level of 95%. Note the different color scales for inactive and active plots.

land. Conversely, during active phases, the strongest signal in mean rain rate was observed over the surrounding ocean, specifically to the west of Luzon.

In particular, the highest mean rain rate values observed during active periods were located to the southwest of Luzon. Farther north, where the flow turned more southerly and parallel to the coast, the mean precipitation rate was reduced. Rainfall also decreased toward the west edge of the map as distance increases from the coast. These two observations suggest that convergence of the monsoon flow with some coastal feature (land breeze, cold pool, etc.) may play a role in generating the offshore precipitation. It should be mentioned that there was still precipitation over the mountain peaks during active phases, although the signal is muted due to the stronger offshore rain signal.

### 3) TRMM UW FEATURES

Figure 5 shows TRMM UW feature counts during inactive BSISO phases (left column), active phases (center column), and the difference in count between inactive and active phases (right column). Deep convective cores (DCC) appeared more frequently over land during inactive phases, consistent with the increased solar heating and instability discussed earlier. Over the ocean, DCCs and wide convective cores (WCC) were generally infrequent during both inactive and active phases. WCCs were slightly more common over the ocean during active phases, particularly off the west coast of Mindoro and Panay (the two smaller islands to the S and SSW of Luzon). A significant increase in both broad stratiform regions (BSR) and isolated shallow echoes (ISE) is apparent to the west of Luzon during

active BSISO phases. Combining this information with the rain rate plots in Fig. 4, one can conclude that the increase in rainfall observed to the west of Luzon was primarily due to large stratiform systems and small raining cells, rather than intense convection. These large stratiform systems must originate from deep convection at some point, so this agrees with the increase in WCCs (and to a lesser extent DCCs) observed over the ocean during active phases.

### c. Diurnal cycle

#### 1) RAINFALL

To gain a sense of the diurnal cycle of rain, Hovmöller diagrams of mean rain rate during inactive and active phases are shown in Fig. 6. During inactive phases, heavy rain developed over the mountains around 1300 LT and persisted until 2100 LT before dissipating. Precipitation then redeveloped offshore at 0300 LT and persisted through the early morning. This nighttime/early morning precipitation maximum over the ocean has been widely observed and studied in the tropics (Kraus 1963; Ruppert et al. 2013; Yang and Smith 2006), and is thought to be more pronounced during convectively active periods (Sakaeda et al. 2018). During active BSISO phases, the diurnal cycle over land was once again very clear. In this case, the afternoon terrain-based convection appeared to move westward off the coast between 1800 and 0000 LT. While the signal of offshore-propagating rainfall only extended to approximately 118°E, rainfall over the open ocean was frequent at all hours. Thus, the increase in rain over the ocean during active phases appears to be due to a combination of offshore movement of land-convection

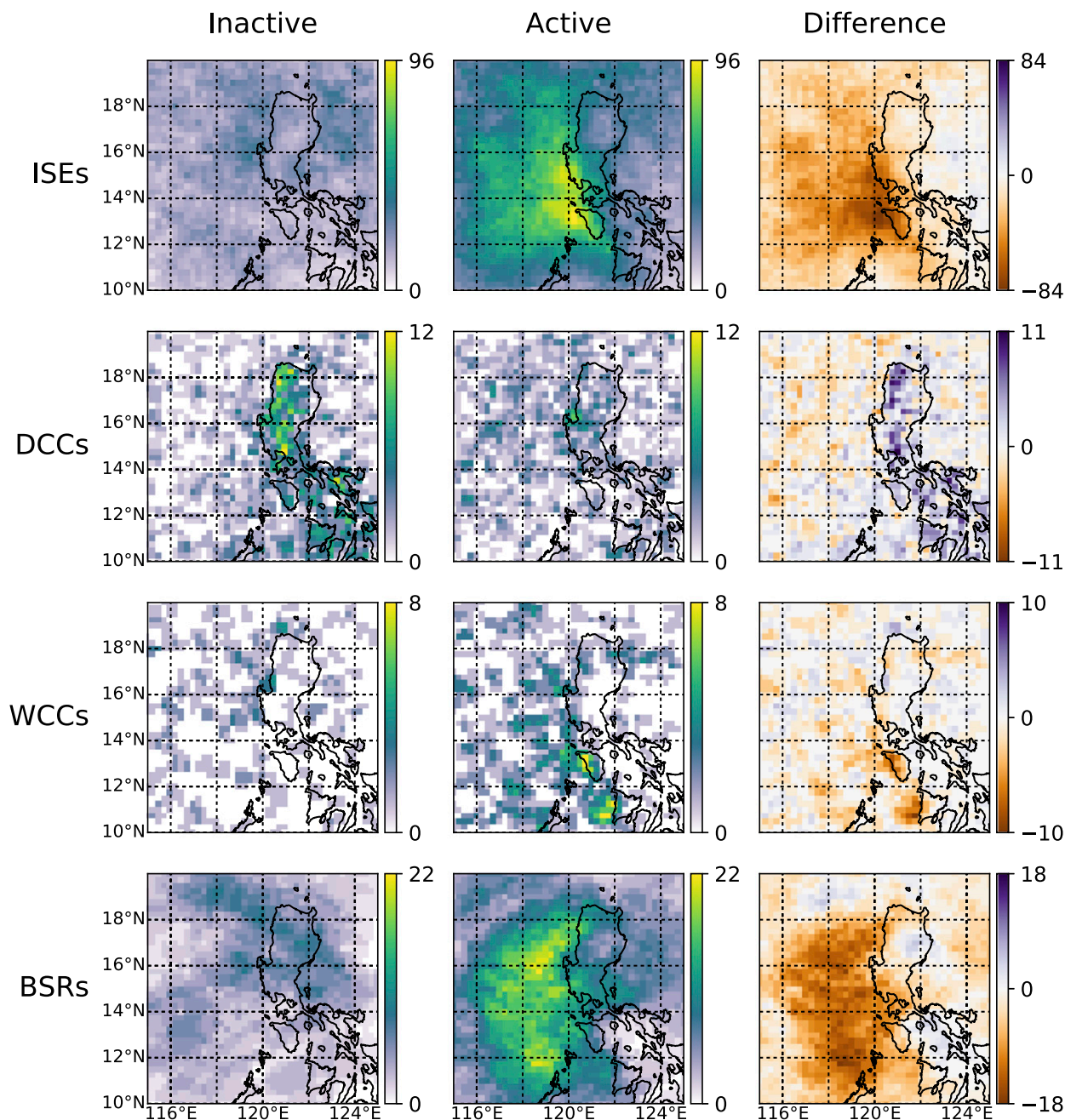


FIG. 5. TRMM UW precipitation feature classification count during (left) inactive and (center) active BSISO phases, and (right) the inactive–active count difference. In the difference plots, blue pixels/positive numbers indicate that more of those features were observed during inactive BSISO phases, brown pixels/negative numbers indicate more were observed during active BSISO phases.

and precipitation which develops independently over the water.

## 2) PRECIPITATION FEATURES

The TRMM/GPM PF database was separated by time-of-day and BSISO phases to analyze the diurnal characteristics of raining systems during different activity

periods. Specifically, 30-dBZ echo heights (Fig. 7), lightning flash rates (Fig. 8), and PF area (Fig. 9) were examined. The 30-dBZ echo heights and lightning flash rates provide a measure of the intensity of the storms and strength of the convective updrafts (Petersen et al. 1996; Zipser and Lutz 1994), while PF sizes can give a sense of the organization and mode

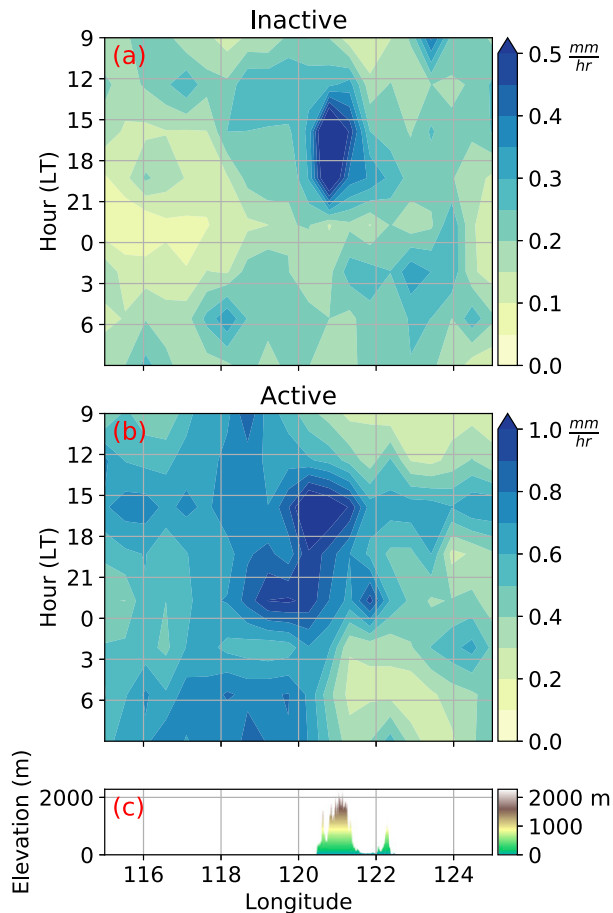


FIG. 6. Hovmöller diagrams of unconditional mean rain rate during (a) inactive and (b) active BSISO phases. Note the different color scales for inactive and active plots. Topography along the 17°N parallel is plotted in (c), as collected from the Shuttle Radar Topography Mission.

of precipitation systems (i.e., large MCS's versus small isolated convective cells). Although several PF characteristics analyzed here are analogous to the various TRMM UW feature types discussed in section 2b(3), the diurnal variation of these characteristics discussed here merits a separate section.

During inactive BSISO phases, deep convection with relatively high flash rates was frequent in the afternoon (1500–1800 local time) over land. The increased instability over land during inactive phases [see section 2b(1)] promoted intense updrafts and stronger storms. The majority of these storms were relatively small in size ( $<2000 \text{ km}^2$ ), with a few larger features ( $>10000 \text{ km}^2$ ) appearing by 1800 LT. This may be a result of isolated convection which initiated over the mountains in the early afternoon, and then merged into larger complexes as the day progressed. Over the SCS to the west, convection

was typically weaker than over land, indicated by lower 30-dBZ heights and lower lightning flash rates. The strongest overocean PFs occurred to the west of Luzon during the overnight/early morning hours (0000–0600 LT).

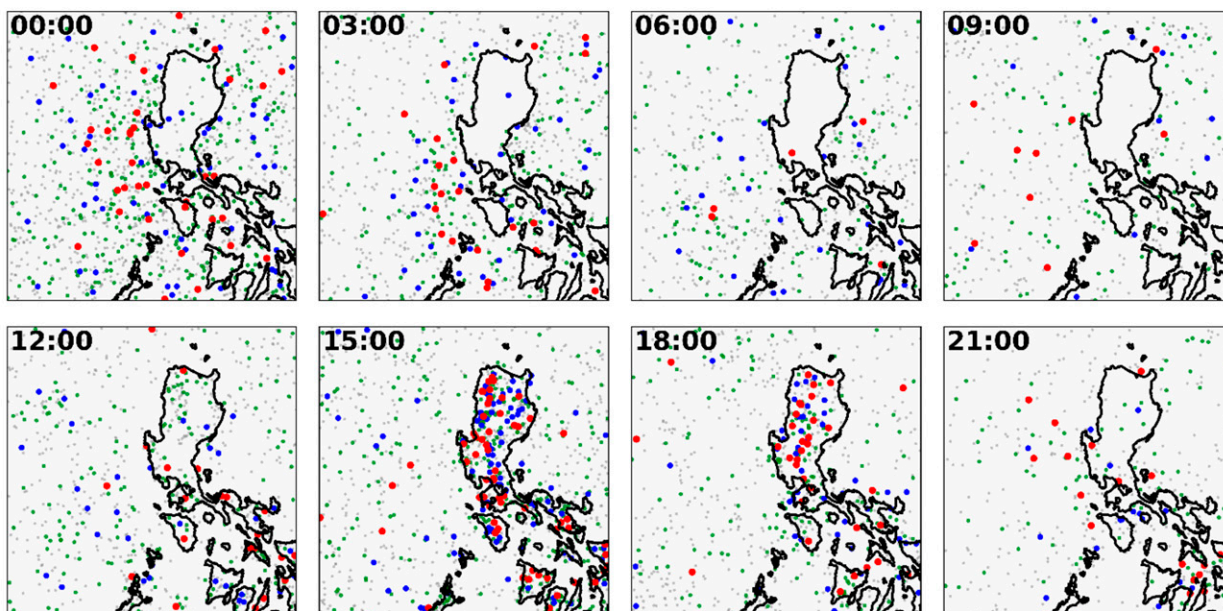
During active BSISO phases, enhanced cloud shading is expected to dampen instability generated over land, thereby reducing the likelihood of intense afternoon convection. However, a diurnal cycle was still noted over land even during active phases, albeit with slightly weaker storms (again denoted by lower 30-dBZ echo heights and reduced lightning flash rates) compared to inactive periods. This was also seen in the Hovmöller diagrams in Fig. 6. As mentioned previously, other studies have shown the importance of the diurnal cycle of land precipitation in enhancing offshore convection in other regions. So, it is important to note that a diurnal cycle still existed over Luzon even during the active phases of the BSISO. Over the SCS, PFs with moderate 30-dBZ heights and some lightning were more widespread during active conditions compared to inactive. Large raining systems ( $>40000 \text{ km}^2$ ) were also much more frequent throughout the diurnal cycle. This suggests a relative abundance of large monsoon rainbands and MCSs traversing the region during active BSISO phases, owing to increased moisture, surface energy fluxes, and vertical wind shear associated with these phases.

A summary of Figs. 7–9 is given in Fig. 10. An afternoon peak in intense storms (as measured by 30-dBZ echo height and lightning flash rate) can be seen in PFs which occur over land during both inactive and, albeit to a lesser degree, active phases. Note that the mean flash rate values were very low ( $<0.5 \text{ flashes min}^{-1}$ ) because the vast majority of PFs ( $>90\%$ ) had a flash rate of zero (i.e., they did not produce detectable lightning). However, an increase in the mean still indicates an increase in the number of storms which contain lightning. At all times of the day, the mean area of PFs over both land and water is larger during active phases.

### 3) DIURNAL CYCLE OF TRMM UW FEATURES

Hovmöller diagrams of TRMM UW feature classification count are presented in Fig. 11. The predominance of DCCs observed during inactive phases over land occurred during the afternoon hours which agrees with the results of Figs. 7–10, showing storms with the tallest 30-dBZ echo tops and highest lightning flash rates occurred at this time and location. Note that DCCs still occurred over the terrain in the afternoon during active phases (not shown), just not with the same frequency as inactive phases.

### 30 dBZ Echo Heights: Inactive



### 30 dBZ Echo Heights: Active

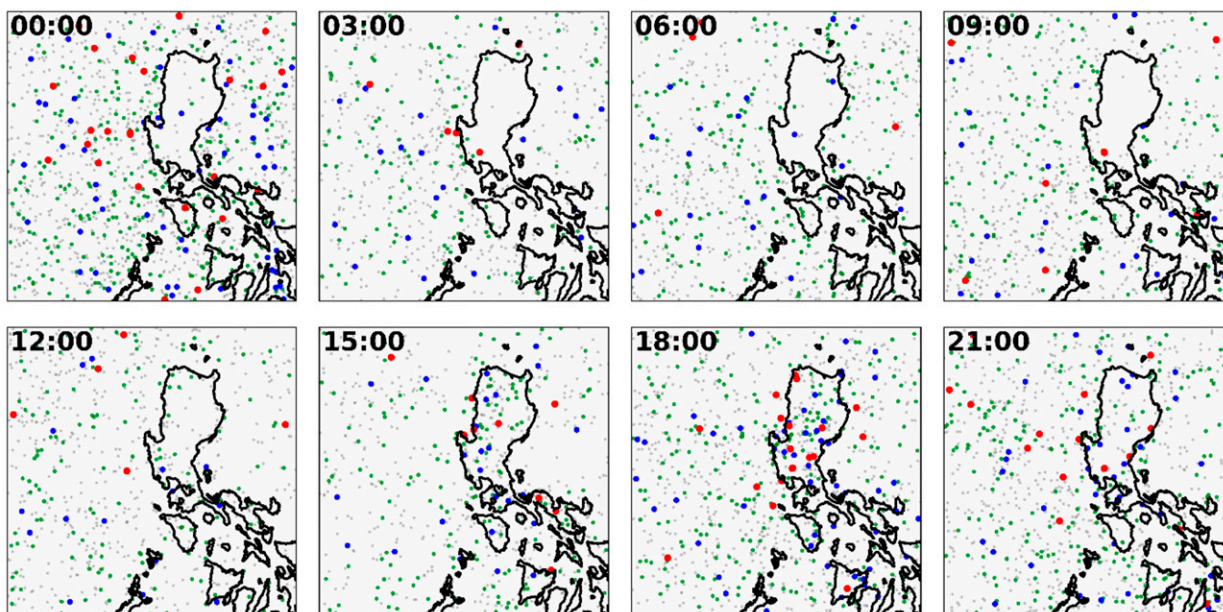


FIG. 7. Scatterplot of 30-dBZ echo heights of TRMM and GPM precipitation features during inactive and active BSISO phases. Dots representing features with higher 30-dBZ echo heights (blues and reds) are also enlarged for emphasis. Timestamps are in local time (UTC + 8 h).

WCCs again occurred the least frequently, with the majority occurring during active phases just along and to the west of the coastline around 120°E. Importantly, a distinction can now be made between the timing of ISEs

and BSRs. While Fig. 5 suggests that both ISEs and BSRs occurred more frequently to the west of Luzon during active BSISO phases, Fig. 11 shows that the BSRs occurred predominantly between 2100 and 0100 LT,

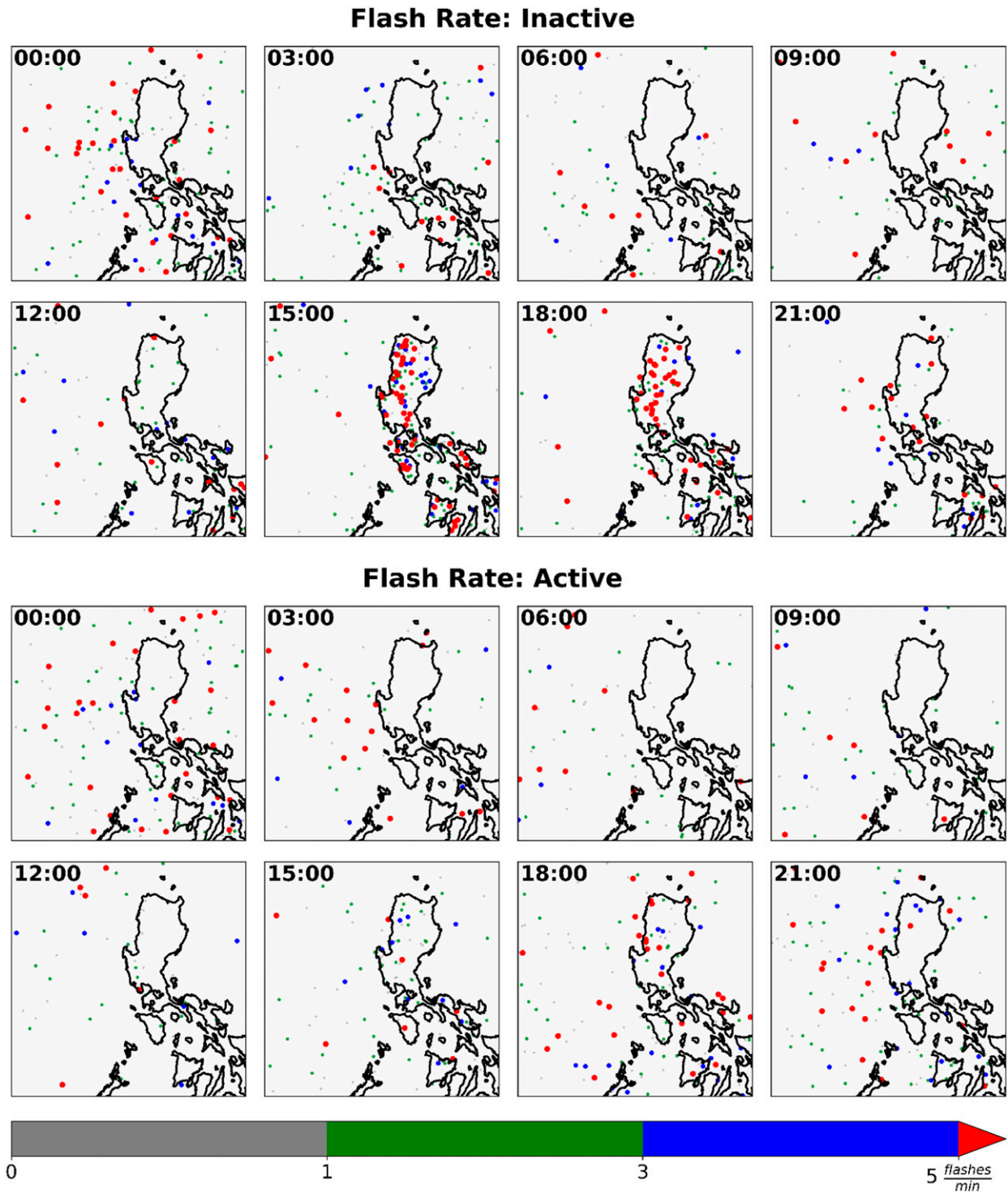
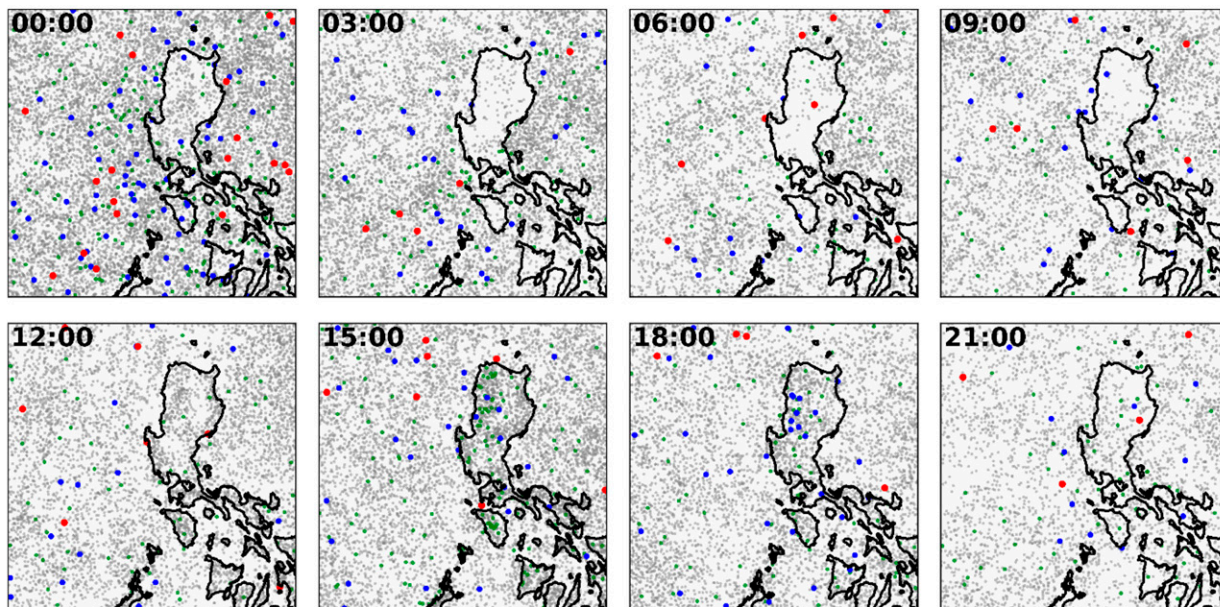


FIG. 8. Scatterplot lightning flash rates of TRMM precipitation features during inactive and active BSISO phases. Dots representing features with higher flash rates (blues and reds) are also enlarged for emphasis. Timestamps are in local time (UTC + 8 h).

**PF Area: Inactive**



**PF Area: Active**

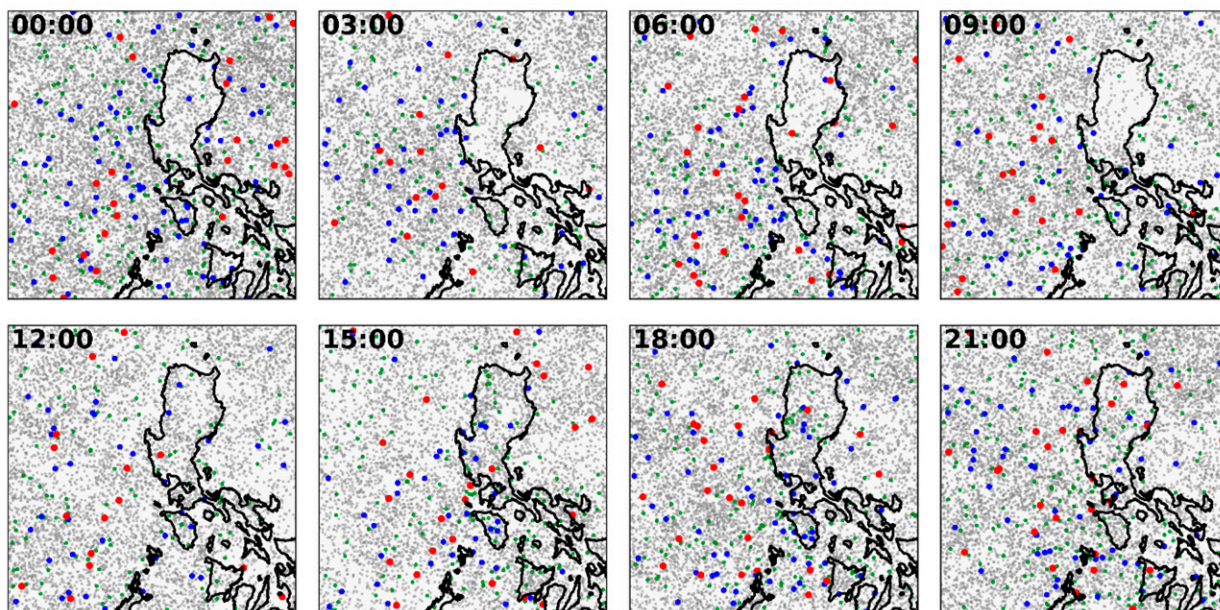


FIG. 9. Scatterplot area of TRMM precipitation features during inactive and active BSISO phases. Dots representing features with larger areas (blues and reds) are also enlarged for emphasis. Timestamps are in local time (UTC + 8 h).

while ISEs generally occurred around the clock (with local maxima between 0500–0800 LT and 1700–2300 LT). The location of this maximum of active phase BSRs and WCCs support offshore movement of afternoon

land-based thunderstorms, which grew in area and develop stratiform raining areas as they moved westward. ISEs appeared to show less of a diurnal cycle, suggesting that these small warm rain showers were

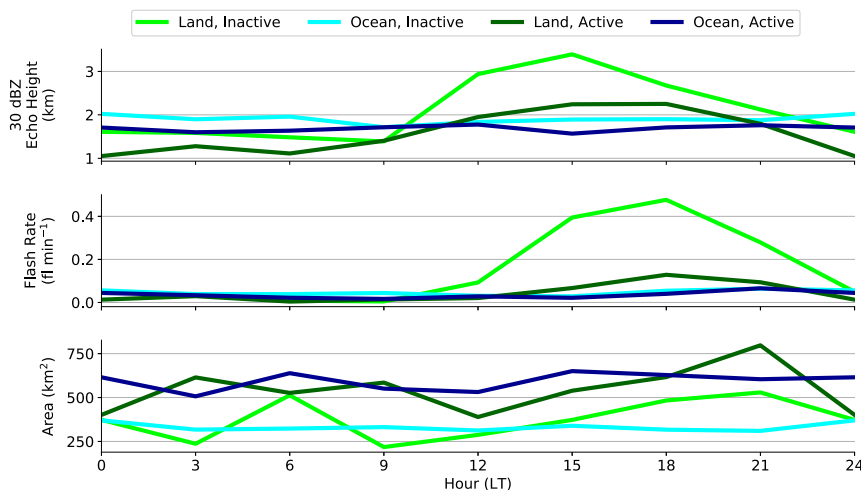


FIG. 10. Mean values of (top) PF 30-dBZ echo height, (middle) flash rate, and (bottom) area as a function of time, composited by location of the PF (land/ocean) and BSISO phase.

ubiquitous to the warm, moist oceanic atmosphere during active phases.

#### 4) VERTICAL STRUCTURE

While rainfall information is useful to determine the location of precipitation, little can be gleaned in terms of the structure of the convection from these data alone. Toward this goal, the vertical structure of precipitating systems was analyzed using reflectivity profiles from TRMM PR and GPM KuPR across different BSISO phases and the diurnal cycle. Figure 12 depicts 4-hourly histograms of the height of minimum detectable echo (MDE;  $\sim 17$  dBZ for TRMM PR and GPM KuPR) along a longitudinal band across our study region during inactive and active phases. Because data are gathered across a longitudinal band, it was desirable for the coastline in this band to run approximately north–south, to avoid mixing radar data from the land and sea. For this reason, only reflectivity profiles within  $16^{\circ}$ – $18^{\circ}$ N were compiled in this analysis. This domain corresponds with the region where the tallest mountain peaks are located.

In general, maximum MDE heights occurred most frequently over the elevated terrain of Luzon. Evidently the orographic lifting along with strong daytime instability produced the updrafts needed for deep convective cores. Very tall afternoon storms were more frequent during inactive phases than active phases over the mountains (57% more MDE heights over 10 km from 1200–2000 LT,  $120^{\circ}$ – $122^{\circ}$ E) corresponding with the greater instability shown previously. The out-of-phase relationship between afternoon land-based and overnight ocean-based precipitation (Kraus 1963; Ruppert et al. 2013; Yang and Smith 2006) was clearly noted

during inactive phases. During active phases, westward offshore movement of the afternoon convection was once again apparent, with a strong precipitation signal moving from  $121^{\circ}$ E at 1400 LT to  $118^{\circ}$ E by 0000 LT, as well as a general persistence of precipitation over the ocean around the clock.

Median vertical profiles of reflectivity over land and ocean were calculated for inactive and active BSISO phases. From these, profiles of reflectivity anomalies were produced by taking the difference between each profile and a mean of the four profiles (Fig. 13). For this calculation, reflectivity was first converted to linear units of  $Z$ , and then converted back to log units of dBZ. Reflectivity was left in log units (dBZ) during the subtraction to calculate anomalies, however qualitatively similar results are obtained using linear units. The deepest and strongest convection was once again noted over the land during inactive phases. Anomalously high reflectivity was seen at the lower and upper levels. A strong melting layer signature was present around the freezing level (5 km) in the oceanic active BSISO profile. During active periods, large, organized convective systems moved over the ocean with mature stratiform regions (agreeing with Xu and Rutledge 2018). Part of this may be from land-based convection which grew upscale as a mature MCS into the SCS, or from convection which originated elsewhere in the SCS before moving into the domain. Conversely, the overland inactive reflectivity anomaly profile had lower values around the freezing level, consistent with convection being more dominant than stratiform precipitation.

To see how these vertical profiles of reflectivity changed through the day, mean profiles from TRMM PR and GPM KuPR were composited by time of day,

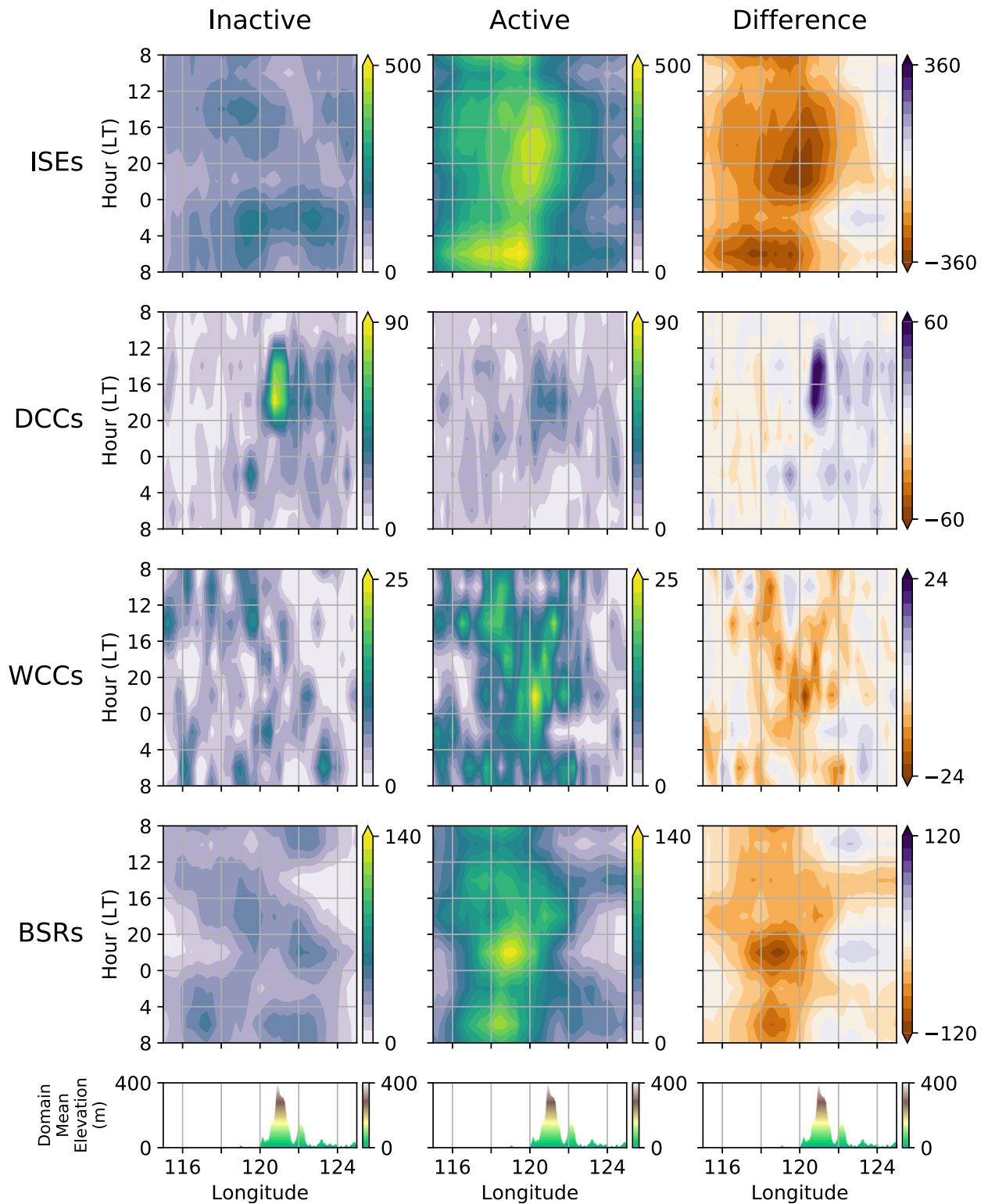


FIG. 11. As in Fig. 5, but as Hovmöller diagrams with classification counts summed up from 10° to 20°N for each longitude bin. Domain-mean topography height, as collected from the Shuttle Radar Topography Mission is plotted in the bottom row.

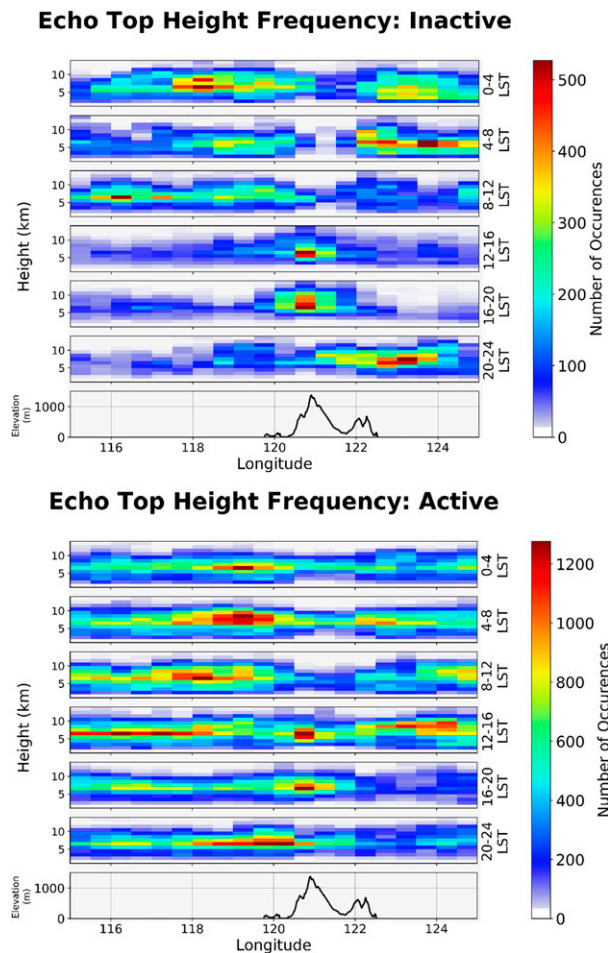


FIG. 12. Echo top height frequency between  $115^{\circ}$ – $125^{\circ}$ E and  $16^{\circ}$ – $18^{\circ}$ N during inactive and active BSISO phases. Histograms are tabulated in 4-hourly bins. Note the different color scales for inactive and active plots. Topography data collected from the from the Shuttle Radar Topography Mission.

BSISO activity, and whether the profile was obtained over land or ocean. These profiles were further divided into convective and stratiform profiles, as determined by the algorithms within the 2A25 and 2A-Ku products from TRMM and GPM, respectively. The results (Figs. 14 and 15) paint a similar picture to what has been discussed previously. Over land during inactive phases, the mean convective profile during the afternoon (1200–2000 LT, orange line) was about 3–5 dBZ higher (statistically significant below 10 km) than the mean profile during the night/early morning hours (0000–0800 LT, blue line), suggesting a significant diurnal cycle in convection. In this sense, a diurnal cycle was also seen in the mean convective profiles over land during active phases, although the difference between profiles was lessened (still significant between 6 and 9 km), owing to the reduced solar heating and instability.

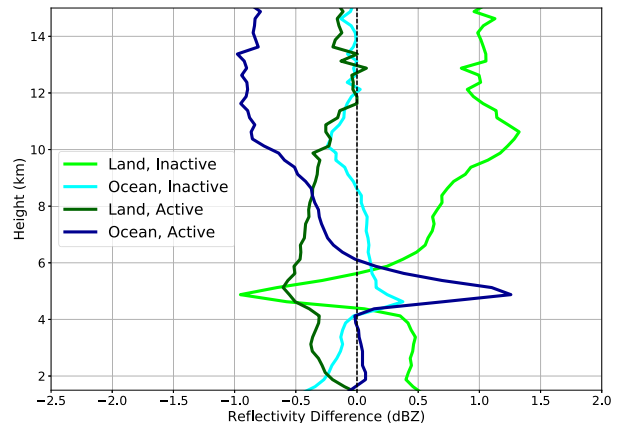


FIG. 13. Vertical profiles of reflectivity anomalies from TRMM PR and GPM KuPR, composited by BSISO activity and whether the profiles were measured over the land or ocean.

For stratiform profiles, there was only a minor difference between the afternoon and night/early morning mean profiles regardless of BSISO phase or land/ocean location. The one exception to this was over land during inactive BSISO phases. Here, the “shoulder” around 5 km that was apparent in all other profiles was not present in the afternoon profile (orange line). This “shoulder” represents a melting layer signature and is manifested by the relatively high reflectivity of large, water-coated, melting snow aggregates which were present in this region. A strong melting layer signature requires the steady phase transition of falling hydrometeors across the freezing level. Reflectivity profiles in convection typically do not exhibit this feature (Fig. 14) due to the updrafts within convection carrying particles upward across the  $0^{\circ}\text{C}$  isotherm. Therefore, the lack of a melting layer signature in the mean afternoon stratiform reflectivity profile over land during inactive phases suggests that the precipitation was, in reality, more convective in nature. We expect the afternoon precipitation over land during inactive phases to be predominately convective (based on the increased instability and nature of precipitation features observed), so this is consistent with the lack of a stratiform melting signature.

#### d. GPM radar case studies

To this point, only broad statistics on the overall nature of precipitation and rainfall have been presented. Although these statistics are certainly useful in capturing the overall nature of convective variability in the region, it is also valuable to examine individual cases of convection in the region to provide context and verification to the conclusions drawn previously. Toward that end, we discuss several examples of individual

## Mean Vertical Profiles of Convective Reflectivity

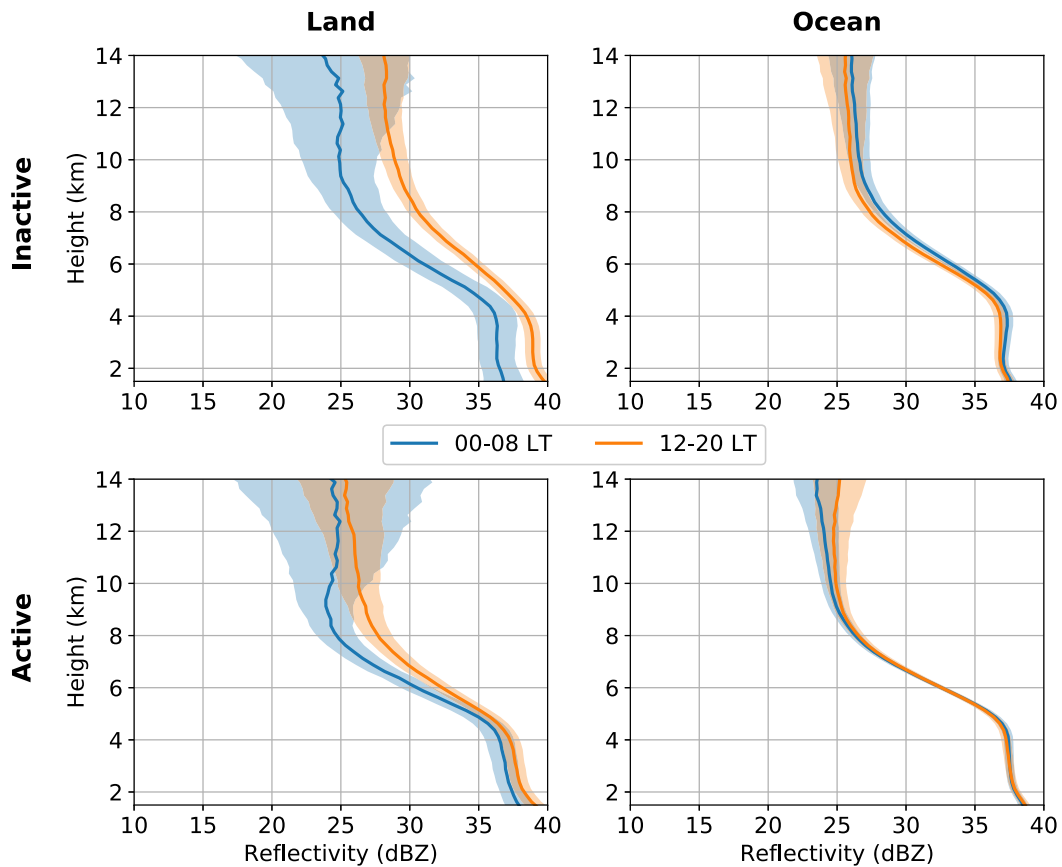


FIG. 14. Mean profiles of reflectivity in convective precipitation composited by time of day, BSISO activity, and whether the profiles were measured over the land or ocean. Shaded regions cover the 95% confidence interval according to a two-tailed Student's  $t$  test.

overpasses from GPM KuPR, along with the atmospheric conditions they occurred in. Unfortunately, GPM makes about two passes over the study region a day, on average, and therefore the full diurnal evolution of a single convective system cannot be captured. Here, although three examples will be given from different periods in the diurnal cycle, they should be thought of as separate examples of what convection looks like at a given time, rather than showcasing the evolution of a single system. Atmospheric sounding data in this section was taken from the city of Laoag, which is marked with a star in Fig. 1.

Figures 16a and 16b show an overpass that occurred during the afternoon of an inactive BSISO phase. Recall from previous discussion that this is when the most intense storms are expected over land. Indeed, this overpass captured several clusters of storms whose cores exceeded 50 dBZ, with echo tops up to 14 km above sea level. The storms were generally located over the

mountainous regions of Luzon. The sounding in Fig. 17a shows a tall, “skinny” instability (low normalized CAPE, see Blanchard 1998) profile with surface temperatures already exceeding 30°C despite this sounding being launched at 0800 LT. Winds were light throughout the mid- to lower atmosphere, with only a weak southwesterly monsoon flow at the surface (as is expected during inactive BSISO phases). The atmosphere likely grew more unstable throughout the day as surface heating continued, leading to conditions which were ripe for convection to form by the afternoon.

Figures 16c and 16d show a late-afternoon overpass which occurred during an active BSISO period. A large convective complex was located along and to the west of the coast of Luzon. A mix of both deep convection and stratiform rain with a well-defined melting layer signature is evident in the cross section (Fig. 16d, also verified by the DPR rain-type classification algorithm). Although it cannot be determined exactly how this

## Mean Vertical Profiles of Stratiform Reflectivity

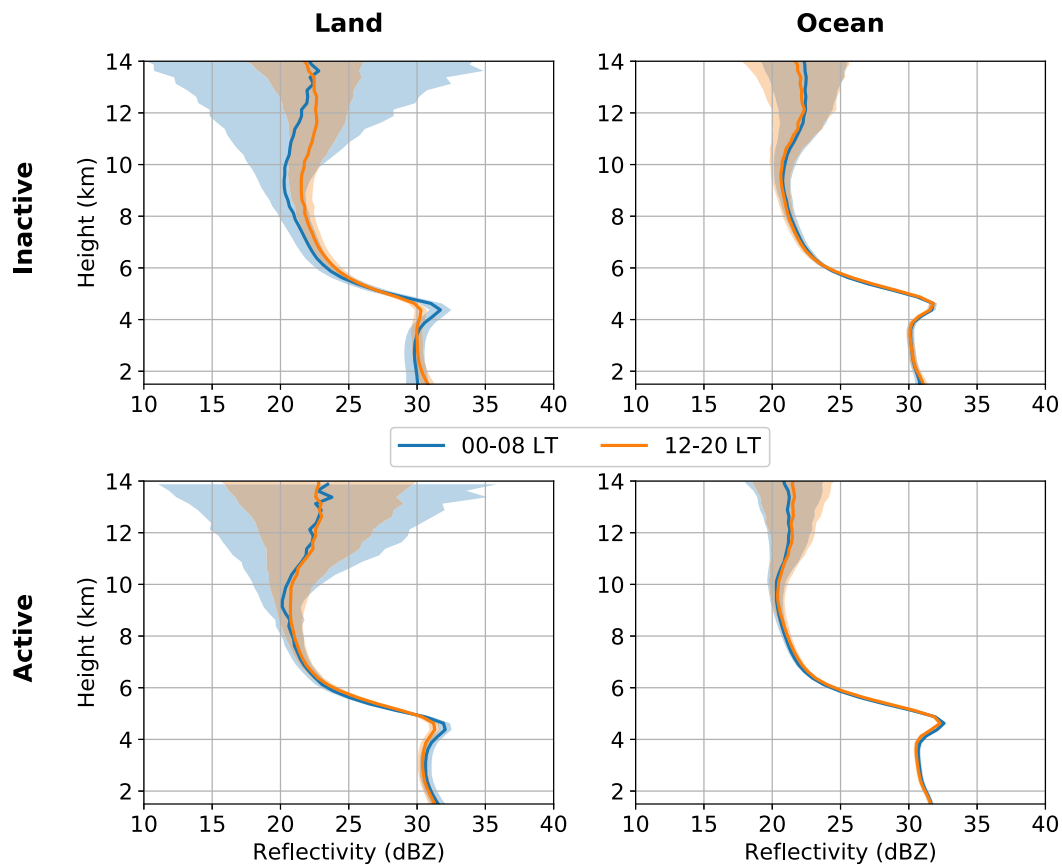


FIG. 15. Mean profiles of reflectivity in stratiform precipitation composited by time of day, BSISO activity, and whether the profiles were measured over the land or ocean. Shaded regions cover the 95% confidence interval according to a two-tailed Student's  $t$  test.

complex formed, it is plausible that it originated from isolated convection which formed in the afternoon over the terrain and grew upscale as it moved offshore. The large wind shear evident in the sounding taken earlier that day (Fig. 17b) would aid in the organization and maintenance of this system (Alfaro and Coniglio 2018; Coniglio et al. 2006; Lang et al. 2007; Moncrieff and Liu 1999; Saxen and Rutledge 2000; Thorpe et al. 1982; Zheng et al. 2013). Regardless of its formation, the morphology, timing, and location of this storm all agree with Fig. 11, which shows an increase in the frequency of BSRs and WCCs along the west coast of Luzon in the late afternoon and evening.

Finally, an early morning GPM overpass during an active BSISO phase (Figs. 16e,f) shows a mix of scattered convection and isolated small warm rain cells. Although deeper convection was present in the area, a cross section was taken through the small cells to illustrate the shallow nature of these features. Recall that Fig. 11 demonstrates the ubiquitous nature of these

types of features during active phases over the ocean. Figure 17c shows these cells formed in a moist atmosphere (69 mm of precipitable water), with strong low-level winds. ERA reanalysis shows that surface sensible and latent heat fluxes over the water were one to three standard deviations above the climatological mean at this time (not shown). Although none of the storms captured by this overpass were particularly intense (only echo tops reach above 10 km), the copious amounts of moisture and high level of energy flux off the ocean surface was sufficient to support widespread precipitation in the early morning hours.

### 3. Summary and discussion

This study primarily examined the characteristics of precipitation in and around the island of Luzon during the boreal summer. Using high-resolution satellite radar data, surface wind measurements, and reanalysis of meteorological variables, precipitation intensity,

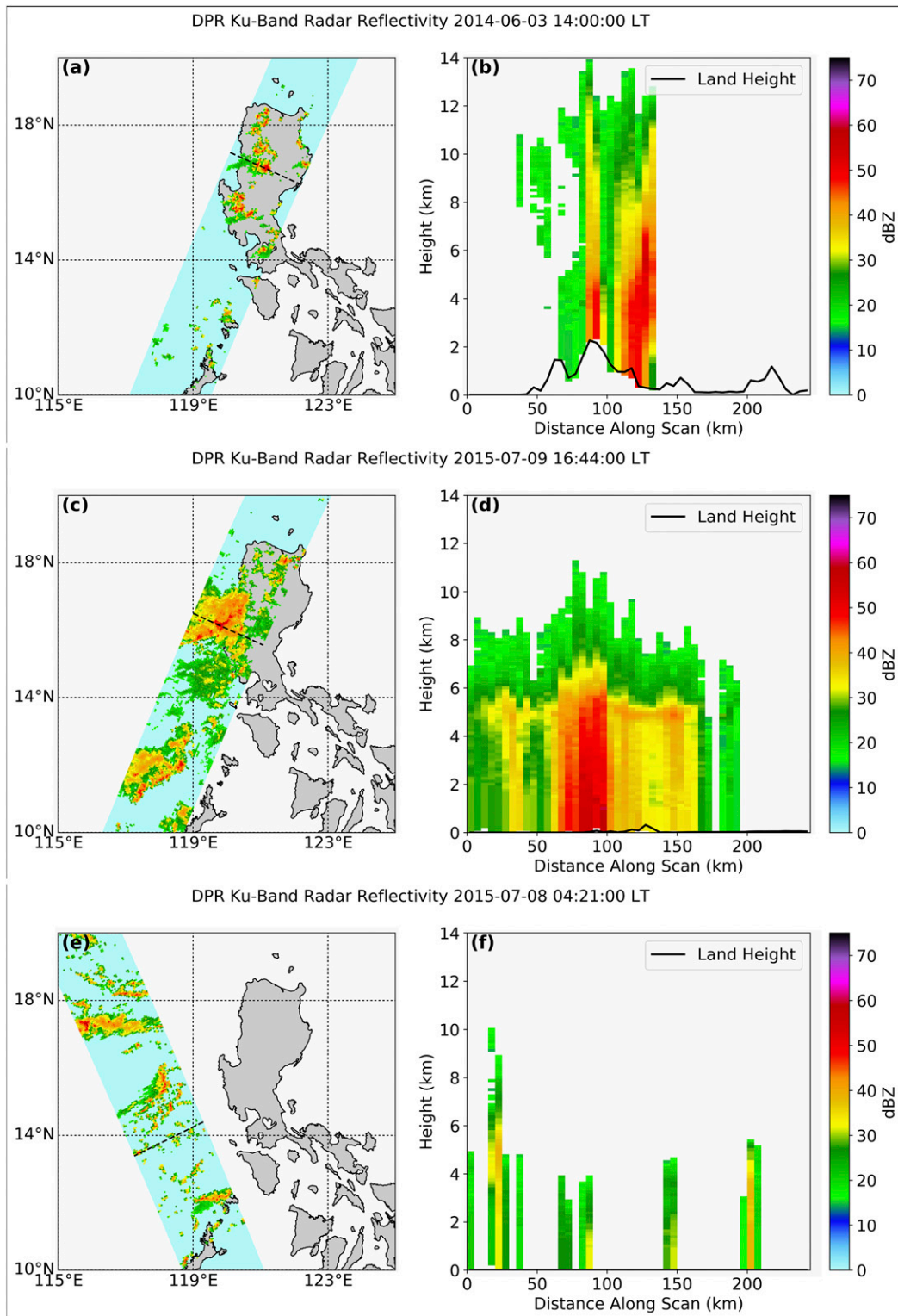


FIG. 16. DPR Ku-band radar (a),(c),(e) composite reflectivity and (b),(d),(f) cross-swath cross sections. The location of the cross sections on the right are marked by the dashed black line in the corresponding figure on the left. Terrain height data from the Shuttle Radar Topography Mission.

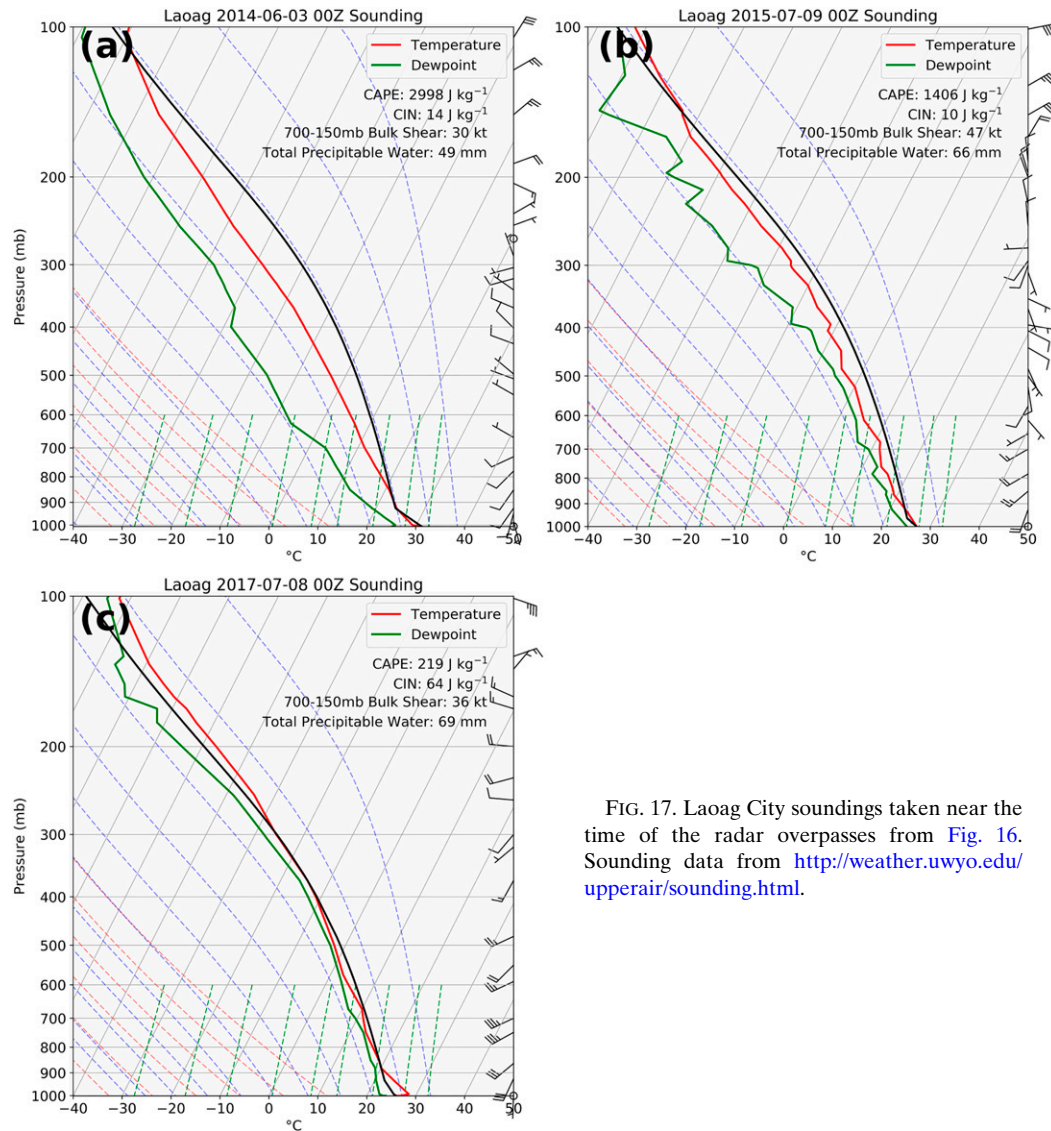


FIG. 17. Laoag City soundings taken near the time of the radar overpasses from Fig. 16. Sounding data from <http://weather.uwyo.edu/upperair/sounding.html>.

morphology, frequency, and location were all examined. Satellite precipitation estimates showed a distinct maximum in precipitation off the west coast of the island. The BSISO, a main driver of intraseasonal variability around Luzon in the boreal summer, was shown to have significant impact on the amount and characteristics of offshore precipitation.

During inactive phases of the BSISO, a strong diurnal cycle existed over land. Between 1500 and 2000 LT, strong, deep convection frequently occurred over the high terrain of Luzon. This was evidenced by higher mean rain rates observed by TRMM PR and GPM KuPR, TRMM PFs with larger lightning flash rates and greater echo top heights, as well as a sharp increase in the number of DCCs. Furthermore, mean vertical profiles of reflectivity over land during inactive phases

featured strong low- and midlevel echoes during the day, in the absence of a well-defined radar bright band (suggesting the precipitation was predominately convective in nature). Over ocean during inactive phases, precipitation was reduced, and the frequency of BSRs was at a minimum. This agrees with previous work, where inactive phases were shown to be associated with reduced cloud cover, increased instability, and localized but intense thunderstorms over land (Ho et al. 2008; Xu and Zipser 2012).

During active phases, the diurnal cycle over land was weakened somewhat, and the afternoon land-based thunderstorms were weaker and fewer in number. Importantly, however, the over land diurnal cycle did not completely vanish. There was still evidence of stronger PFs, increased low-level reflectivity, and a maximum in DCCs over the land in the afternoon during

active phases. Active phases also brought a significant increase in the amount of offshore precipitation. The mean rain rate over the SCS west of Luzon was approximately 2–3 times higher during active phases than inactive phases throughout the day. In particular, offshore rainfall was maximized just off the coast from 2000 to 0000 LT. The period also corresponded with a maximum in the frequency of WCCs and BSRs. The location and timing of these large, organized systems suggests that they may have originated from isolated convection over the terrain, which formed in the afternoon and then moved westward over the ocean and grew upscale into organized complexes as the day progressed. Conversely, ISEs were shown to occur frequently around the clock, with a less prominent diurnal cycle. The omnipresence of these small warm rain cells speaks toward the nature of the monsoon environment, with moisture-laden air and strong low-level winds blowing over warm SSTs, leading to an atmosphere which was very conducive to precipitation.

Previous field work (Houze et al. 1981; Mapes et al. 2003; Nesbitt et al. 2008; Ruppert et al. 2013; Xu et al. 2012) has shown that the diurnal cycle is a key component in creating offshore precipitation. Therefore, a key finding of this study was that a diurnal cycle in convection existed over the land during both inactive and active phases, despite the reduction in solar insolation during the latter. Curiously, although the diurnal cycle was stronger during inactive phases, offshore precipitation was reduced. This suggests that a strong monsoon flow (along with other conditions brought about by an active BSISO) may also be a key ingredient to generating offshore precipitation. Mechanisms outlined in previous studies for offshore precipitation involving convergence with a land/sea breeze (WMONEX, Houze et al. 1981), katabatic winds (TiMREX, Ruppert et al. 2013), or cold pool (TiMREX, Xu et al. 2012) seem plausible, as the existence of a strong monsoon flow would provide the onshore winds to converge with any of these seaward features. This supports the finding in Natoli and Maloney (2019) that offshore movement of convection is maximized in the transition from inactive to active phases. During these periods, solar insolation is still pronounced (generating instability, sea-breeze circulations, and a stronger diurnal cycle over land); however, the influences of the active BSISO (increased moisture, stronger low-level winds) also begin to materialize. Although not studied in this paper, this transition period may indeed be the “Goldilocks” zone for offshore precipitation.

Importantly, all of the studies above (excluding Natoli and Maloney 2019) had direct measurements from field campaigns to corroborate their proposed mechanisms. These mechanisms all involve mesoscale (or submesoscale) features, which evolve on the order of hours. These processes

cannot be resolved with satellite and reanalysis data alone, thus it is beyond the scope of this study to propose an exact mechanism through which the offshore precipitation maximum observed in Luzon is generated. To fully resolve the details of the convergence boundaries and local wind features which are likely important, in situ measurements with high spatiotemporal resolution are required. The aim of this study was to provide some a priori knowledge of the characteristics of convection in the region, should such observations ever be made.

*Acknowledgments.* This research was funded by the Office of Naval Research Grant N00014-16-1-3092 (supporting all three authors) and NASA Grant NNX16AD85G (supporting S. Rutledge). TRMM and GPM satellite data can be downloaded from NASA Goddard Earth Sciences Data and Information Services Center ([https://disc.gsfc.nasa.gov/datacollection/TRMM\\_2A25\\_7.html](https://disc.gsfc.nasa.gov/datacollection/TRMM_2A25_7.html), [https://disc.gsfc.nasa.gov/datasets/GPM\\_2AKu\\_V06/summary](https://disc.gsfc.nasa.gov/datasets/GPM_2AKu_V06/summary)). TRMM and GPM precipitation features can be downloaded at <http://atmos.tamucc.edu/trmm/>. The TRMM UW database can be accessed at <http://trmm.atmos.washington.edu/>. Special thanks to Dr. Kristen Rasmussen for her assistance in obtaining and analyzing the TRMM UW database. CCMP wind estimates are available at <http://www.remss.com/measurements/ccmp/>. ERA-Interim reanalysis data can be accessed at <https://www.ecmwf.int/en/forecasts/datasets/reanalysis-datasets/era-interim>. Shuttle Radar Topography Mission data available at <https://dds.cr.usgs.gov/srtm/>.

## REFERENCES

- Alfaro, D. A., and M. C. Coniglio, 2018: Discrimination of mature and dissipating severe-wind-producing MCSs with layer-lifting indices. *Wea. Forecasting*, **33**, 3–21, <https://doi.org/10.1175/WAF-D-17-0088.1>.
- Atlas, R., R. N. Hoffman, J. Ardizzone, S. M. Leidner, J. C. Jusem, D. K. Smith, and D. Gombos, 2011: A cross-calibrated, multiplatform ocean surface wind velocity product for meteorological and oceanographic applications. *Bull. Amer. Meteor. Soc.*, **92**, 157–174, <https://doi.org/10.1175/2010BAMS2946.1>.
- Blanchard, D. O., 1998: Assessing the vertical distribution of convective available potential energy. *Wea. Forecasting*, **13**, 870–877, [https://doi.org/10.1175/1520-0434\(1998\)013<0870:ATVDOC>2.0.CO;2](https://doi.org/10.1175/1520-0434(1998)013<0870:ATVDOC>2.0.CO;2).
- Coniglio, M. C., D. J. Stensrud, and L. J. Wicker, 2006: Effects of upper-level shear on the structure and maintenance of strong quasi-linear mesoscale convective systems. *J. Atmos. Sci.*, **63**, 1231–1252, <https://doi.org/10.1175/JAS3681.1>.
- Dee, D. P., and Coauthors, 2011: The ERA-Interim reanalysis: Configuration and performance of the data assimilation system. *Quart. J. Roy. Meteor. Soc.*, **137**, 553–597, <https://doi.org/10.1002/qj.828>.
- Dellaripa, E. M. R., E. D. Maloney, B. A. Toms, S. M. Saleeby, and S. C. van den Heever, 2020: Topographic effects on the Luzon

- diurnal cycle during the BSISO. *J. Atmos. Sci.*, **77**, 3–30, <https://doi.org/10.1175/JAS-D-19-0046.1>.
- Grossman, R. L., and D. R. Durran, 1984: Interaction of low-level flow with the western Ghat Mountains and offshore convection in the summer monsoon. *Mon. Wea. Rev.*, **112**, 652–672, [https://doi.org/10.1175/1520-0493\(1984\)112<0652:IOLLFV>2.0.CO;2](https://doi.org/10.1175/1520-0493(1984)112<0652:IOLLFV>2.0.CO;2).
- Ho, C., M. Park, Y. Choi, and Y. N. Takayabu, 2008: Relationship between intraseasonal oscillation and diurnal variation of summer rainfall over the South China Sea. *Geophys. Res. Lett.*, **35**, L03701, <https://doi.org/10.1029/2007GL031962>.
- Houze, R. A., Jr., S. G. Geotis, F. D. Marks Jr., and A. K. West, 1981: Winter monsoon convection in the vicinity of north Borneo. Part I: Structure and time variation of the clouds and precipitation. *Mon. Wea. Rev.*, **109**, 1595–1614, [https://doi.org/10.1175/1520-0493\(1981\)109<1595:WMCITV>2.0.CO;2](https://doi.org/10.1175/1520-0493(1981)109<1595:WMCITV>2.0.CO;2).
- , K. L. Rasmussen, M. D. Zuluaga, and S. R. Brodzik, 2015: The variable nature of convection in the tropics and subtropics: A legacy of 16 years of the Tropical Rainfall Measuring Mission satellite. *Rev. Geophys.*, **53**, 994–1021, <https://doi.org/10.1002/2015RG000488>.
- Iguchi, T., and R. Meneghini, 2016: GPM DPR Ku precipitation profile 2A 1.5 hours 5 km V06. Goddard Earth Sciences Data and Information Services Center (GES DISC), Greenbelt, MD, accessed October 2019, <https://doi.org/10.5067/GPM/DPR/Ku/2A/06>.
- , T. Kozu, R. Meneghini, J. Awaka, and K. Okamoto, 2000: Rain-profiling algorithm for the TRMM precipitation radar. *J. Appl. Meteor.*, **39**, 2038–2052, [https://doi.org/10.1175/1520-0450\(2001\)040<2038:RPAFTT>2.0.CO;2](https://doi.org/10.1175/1520-0450(2001)040<2038:RPAFTT>2.0.CO;2).
- Johnson, R. H., and P. E. Ciesielski, 2013: Structure and properties of Madden–Julian oscillations deduced from DYNAMO sounding arrays. *J. Atmos. Sci.*, **70**, 3157–3179, <https://doi.org/10.1175/JAS-D-13-065.1>.
- Kiladis, G. N., J. Dias, K. H. Straub, M. C. Wheeler, S. N. Tulich, K. Kikuchi, K. M. Weickmann, and M. J. Ventrice, 2014: A comparison of OLR and circulation-based indices for tracking the MJO. *Mon. Wea. Rev.*, **142**, 1697–1715, <https://doi.org/10.1175/MWR-D-13-00301.1>.
- Kraus, E. B., 1963: The diurnal precipitation change over the sea. *J. Atmos. Sci.*, **20**, 551–556, [https://doi.org/10.1175/1520-0469\(1963\)020<0551:TDPcot>2.0.CO;2](https://doi.org/10.1175/1520-0469(1963)020<0551:TDPcot>2.0.CO;2).
- Krishnamurti, T., S. Cocks, R. Pasch, and S. Low-Nam, 1983: Precipitation estimates from rain gauge and satellite observations, summer MONEX. FSU Rep. 83-7, Department of Meteorology, The Florida State University, 373 pp.
- Kummerow, C., W. Barnes, T. Kozu, J. Shiue, and J. Simpson, 1998: The Tropical Rainfall Measuring Mission (TRMM) sensor package. *J. Atmos. Oceanic Technol.*, **15**, 809–817, [https://doi.org/10.1175/1520-0426\(1998\)015<0809:TTRMMT>2.0.CO;2](https://doi.org/10.1175/1520-0426(1998)015<0809:TTRMMT>2.0.CO;2).
- Lang, T. J., D. A. Ahijevych, S. W. Nesbitt, R. E. Carbone, S. A. Rutledge, and R. Cifelli, 2007: Radar-observed characteristics of precipitating systems during NAME 2004. *J. Climate*, **20**, 1713–1733, <https://doi.org/10.1175/JCLI4082.1>.
- Lee, J., B. Wang, M. C. Wheeler, X. Fu, D. E. Waliser, and I. Kang, 2013: Real-time multivariate indices for the boreal summer intraseasonal oscillation over the Asian summer monsoon region. *Climate Dyn.*, **40**, 493–509, <https://doi.org/10.1007/s00382-012-1544-4>.
- Leith, C., 1973: The standard error of time-average estimates of climatic means. *J. Appl. Meteor.*, **12**, 1066–1069, [https://doi.org/10.1175/1520-0450\(1973\)012<1066:TSEOTA>2.0.CO;2](https://doi.org/10.1175/1520-0450(1973)012<1066:TSEOTA>2.0.CO;2).
- Liu, C., E. J. Zipser, D. J. Cecil, S. W. Nesbitt, and S. Sherwood, 2008: A cloud and precipitation feature database from nine years of TRMM observations. *J. Appl. Meteor. Climatol.*, **47**, 2712–2728, <https://doi.org/10.1175/2008JAMC1890.1>.
- Lucas, C., and E. J. Zipser, 2000: Environmental variability during TOGA COARE. *J. Atmos. Sci.*, **57**, 2333–2350, [https://doi.org/10.1175/1520-0469\(2000\)057<2333:EVDTCC>2.0.CO;2](https://doi.org/10.1175/1520-0469(2000)057<2333:EVDTCC>2.0.CO;2).
- Mapes, B., and R. A. Houze Jr., 1992: An integrated view of the 1987 Australian monsoon and its mesoscale convective systems. I: Horizontal structure. *Quart. J. Roy. Meteor. Soc.*, **118**, 927–963, <https://doi.org/10.1002/qj.49711850706>.
- , T. T. Warner, and M. Xu, 2003: Diurnal patterns of rainfall in northwestern South America. Part III: Diurnal gravity waves and nocturnal convection offshore. *Mon. Wea. Rev.*, **131**, 830–844, [https://doi.org/10.1175/1520-0493\(2003\)131<0830:DPORIN>2.0.CO;2](https://doi.org/10.1175/1520-0493(2003)131<0830:DPORIN>2.0.CO;2).
- Moncrieff, M. W., and C. Liu, 1999: Convection initiation by density currents: Role of convergence, shear, and dynamical organization. *Mon. Wea. Rev.*, **127**, 2455–2464, [https://doi.org/10.1175/1520-0493\(1999\)127<2455:CIBDCR>2.0.CO;2](https://doi.org/10.1175/1520-0493(1999)127<2455:CIBDCR>2.0.CO;2).
- Natoli, M. B., and E. D. Maloney, 2019: Intraseasonal variability of the diurnal cycle of precipitation in the Philippines. *J. Atmos. Sci.*, **76**, 3633–3654, <https://doi.org/10.1175/JAS-D-19-0152.1>.
- Nesbitt, S. W., D. J. Gochis, and T. J. Lang, 2008: The diurnal cycle of clouds and precipitation along the Sierra Madre Occidental observed during NAME-2004: Implications for warm season precipitation estimation in complex terrain. *J. Hydrometeorol.*, **9**, 728–743, <https://doi.org/10.1175/2008JHM939.1>.
- Ogura, Y., and M. Yoshizaki, 1988: Numerical study of orographic-convective precipitation over the eastern Arabian Sea and the Ghat Mountains during the summer monsoon. *J. Atmos. Sci.*, **45**, 2097–2122, [https://doi.org/10.1175/1520-0469\(1988\)045<2097:NSOOCp>2.0.CO;2](https://doi.org/10.1175/1520-0469(1988)045<2097:NSOOCp>2.0.CO;2).
- Peters, K., C. Jakob, L. Davies, B. Khouider, and A. J. Majda, 2013: Stochastic behavior of tropical convection in observations and a multicloud model. *J. Atmos. Sci.*, **70**, 3556–3575, <https://doi.org/10.1175/JAS-D-13-031.1>.
- Petersen, W. A., S. A. Rutledge, and R. E. Orville, 1996: Cloud-to-ground lightning observations from TOGA COARE: Selected results and lightning location algorithms. *Mon. Wea. Rev.*, **124**, 602–620, [https://doi.org/10.1175/1520-0493\(1996\)124<0602:CTGLOF>2.0.CO;2](https://doi.org/10.1175/1520-0493(1996)124<0602:CTGLOF>2.0.CO;2).
- Ruppert, J. H., Jr., R. H. Johnson, and A. K. Rowe, 2013: Diurnal circulations and rainfall in Taiwan during SoWMEX/TIMREX (2008). *Mon. Wea. Rev.*, **141**, 3851–3872, <https://doi.org/10.1175/MWR-D-12-00301.1>.
- Sakaeda, N., S. W. Powell, J. Dias, and G. N. Kiladis, 2018: The diurnal variability of precipitating cloud populations during DYNAMO. *J. Atmos. Sci.*, **75**, 1307–1326, <https://doi.org/10.1175/JAS-D-17-0312.1>.
- Saxen, T. R., and S. A. Rutledge, 2000: Surface rainfall–cold cloud fractional coverage relationship in TOGA COARE: A function of vertical wind shear. *Mon. Wea. Rev.*, **128**, 407–415, [https://doi.org/10.1175/1520-0493\(2000\)128<0407:SRCCFC>2.0.CO;2](https://doi.org/10.1175/1520-0493(2000)128<0407:SRCCFC>2.0.CO;2).
- Thorpe, A., M. Miller, and M. Moncrieff, 1982: Two-dimensional convection in non-constant shear: A model of mid-latitude squall lines. *Quart. J. Roy. Meteor. Soc.*, **108**, 739–762, <https://doi.org/10.1002/qj.49710845802>.
- Wang, B., and X. Xie, 1997: A model for the boreal summer intraseasonal oscillation. *J. Atmos. Sci.*, **54**, 72–86, [https://doi.org/10.1175/1520-0469\(1997\)054<0072:AMFTBS>2.0.CO;2](https://doi.org/10.1175/1520-0469(1997)054<0072:AMFTBS>2.0.CO;2).
- Wang, Y., W. Tao, and J. Simpson, 1996: The impact of ocean surface fluxes on a TOGA COARE convective system. *Mon. Wea. Rev.*, **124**, 2753–2763, [https://doi.org/10.1175/1520-0493\(1996\)124<2753:TIOOSF>2.0.CO;2](https://doi.org/10.1175/1520-0493(1996)124<2753:TIOOSF>2.0.CO;2).

- Xie, S., H. Xu, N. Saji, Y. Wang, and W. T. Liu, 2006: Role of narrow mountains in large-scale organization of Asian monsoon convection. *J. Climate*, **19**, 3420–3429, <https://doi.org/10.1175/JCLI3777.1>.
- Xu, W., and E. J. Zipser, 2012: Properties of deep convection in tropical continental, monsoon, and oceanic rainfall regimes. *Geophys. Res. Lett.*, **39**, L07802, <https://doi.org/10.1029/2012GL051242>.
- , and S. A. Rutledge, 2018: Convective variability associated with the boreal summer intraseasonal oscillation in the South China Sea region. *J. Climate*, **31**, 7363–7383, <https://doi.org/10.1175/JCLI-D-18-0091.1>.
- , E. J. Zipser, Y. Chen, C. Liu, Y. Liou, W. Lee, and B. Jong-Do Jou, 2012: An orography-associated extreme rainfall event during TiMREX: Initiation, storm evolution, and maintenance. *Mon. Wea. Rev.*, **140**, 2555–2574, <https://doi.org/10.1175/MWR-D-11-00208.1>.
- Yang, S., and E. A. Smith, 2006: Mechanisms for diurnal variability of global tropical rainfall observed from TRMM. *J. Climate*, **19**, 5190–5226, <https://doi.org/10.1175/JCLI3883.1>.
- Yokoi, S., S. Mori, M. Katsumata, B. Geng, K. Yasunaga, F. Syamsudin, Nurhayati, and K. Yoneyama, 2017: Diurnal cycle of precipitation observed in the western coastal area of Sumatra Island: Offshore preconditioning by gravity waves. *Mon. Wea. Rev.*, **145**, 3745–3761, <https://doi.org/10.1175/MWR-D-16-0468.1>.
- , —, F. Syamsudin, U. Haryoko, and B. Geng, 2019: Environmental conditions for nighttime offshore migration of precipitation area as revealed by in situ observation off Sumatra Island. *Mon. Wea. Rev.*, **147**, 3391–3407, <https://doi.org/10.1175/MWR-D-18-0412.1>.
- Zheng, L., J. Sun, X. Zhang, and C. Liu, 2013: Organizational modes of mesoscale convective systems over central East China. *Wea. Forecasting*, **28**, 1081–1098, <https://doi.org/10.1175/WAF-D-12-00088.1>.
- Zipser, E. J., and K. R. Lutz, 1994: The vertical profile of radar reflectivity of convective cells: A strong indicator of storm intensity and lightning probability? *Mon. Wea. Rev.*, **122**, 1751–1759, [https://doi.org/10.1175/1520-0493\(1994\)122<1751:TVPORR>2.0.CO;2](https://doi.org/10.1175/1520-0493(1994)122<1751:TVPORR>2.0.CO;2).
- Zuidema, P., 2003: Convective clouds over the Bay of Bengal. *Mon. Wea. Rev.*, **131**, 780–798, [https://doi.org/10.1175/1520-0493\(2003\)131<0780:CCOTBO>2.0.CO;2](https://doi.org/10.1175/1520-0493(2003)131<0780:CCOTBO>2.0.CO;2).